

AD _____

Award Number: DAMD17-00-1-0408

TITLE: Parallel, Rapid Diffuse Optical Tomography of Breast

PRINCIPAL INVESTIGATOR: Arjun G. Yodh, Ph.D.
Britton Chance

CONTRACTING ORGANIZATION: University of Pennsylvania
Philadelphia, Pennsylvania 19104-3246

REPORT DATE: July 2002

TYPE OF REPORT: Annual

PREPARED FOR: U.S. Army Medical Research and Materiel Command
Fort Detrick, Maryland 21702-5012

DISTRIBUTION STATEMENT: Approved for Public Release;
Distribution Unlimited

The views, opinions and/or findings contained in this report are those of the author(s) and should not be construed as an official Department of the Army position, policy or decision unless so designated by other documentation.

20030214 139

REPORT DOCUMENTATION PAGEForm Approved
OMB No. 074-0188

Public reporting burden for this collection of information is estimated to average 1 hour per response, including the time for reviewing instructions, searching existing data sources, gathering and maintaining the data needed, and completing and reviewing this collection of information. Send comments regarding this burden estimate or any other aspect of this collection of information, including suggestions for reducing this burden to Washington Headquarters Services, Directorate for Information Operations and Reports, 1215 Jefferson Davis Highway, Suite 1204, Arlington, VA 22202-4302, and to the Office of Management and Budget, Paperwork Reduction Project (0704-0188), Washington, DC 20503

1. AGENCY USE ONLY (Leave blank)**2. REPORT DATE**

July 2002

3. REPORT TYPE AND DATES COVERED

Annual (1 Jul 01 - 30 Jun 02)

4. TITLE AND SUBTITLE

Parallel, Rapid Diffuse Optical Tomography of Breast

5. FUNDING NUMBERS

DAMD17-00-1-0408

6. AUTHOR(S)

Arjun G. Yodh, Ph.D.

Britton Chance

7. PERFORMING ORGANIZATION NAME(S) AND ADDRESS(ES)

University of Pennsylvania

Philadelphia, Pennsylvania 19104-3246

E-Mail: yodh@dept.physics.upenn.edu

**8. PERFORMING ORGANIZATION
REPORT NUMBER****9. SPONSORING / MONITORING AGENCY NAME(S) AND ADDRESS(ES)**U.S. Army Medical Research and Materiel Command
Fort Detrick, Maryland 21702-5012**10. SPONSORING / MONITORING
AGENCY REPORT NUMBER****11. SUPPLEMENTARY NOTES****12a. DISTRIBUTION / AVAILABILITY STATEMENT**

Approved for Public Release; Distribution Unlimited

12b. DISTRIBUTION CODE**13. Abstract (Maximum 200 Words) (abstract should contain no proprietary or confidential information)**

During the last year we have experimentally and computationally investigated rapid acquisition and analysis of informationally dense diffuse optical data sets in the parallel plate compressed breast geometry. We have developed and tested a 3-dimensional image reconstruction algorithm for the diffusive wave inverse problem that runs on a parallel computer cluster. This code uses a finite difference method in the forward calculation, a novel Integro-Differential equation, previously developed by this group, in the reconstruction. There has been a significant improvement in our instrumentation and measurement capabilities. A hybrid RF/CW diffuse optical tomography (DOT) system measures limited number of frequency-domain reemission data and significantly larger continuous wave transmission data by a lens coupled CCD simultaneously. The wavelength of the light source is optically switched from 690, 750, 786 and 830 nm and then its position is switched among 45 different positions on the compression plate. The instrument and reconstruction algorithm performance have been tested using small silicone tissue phantoms as a tumor of various size and optical properties suspended into the liquid tissue phantom. The study of the effect of boundary between the matching fluid and breast has been initiated by building and taking measurements from tissue phantoms with breast shape, embedded with small objects with higher absorption or scattering.

14. SUBJECT TERMS

photon migration, photon density waves, near-infrared spectroscopy, image reconstruction, diffuse optical tomography, optical mammography, breast cancer

15. NUMBER OF PAGES

63

16. PRICE CODE**17. SECURITY CLASSIFICATION
OF REPORT**

Unclassified

**18. SECURITY CLASSIFICATION
OF THIS PAGE**

Unclassified

**19. SECURITY CLASSIFICATION
OF ABSTRACT**

Unclassified

20. LIMITATION OF ABSTRACT

Unlimited

NSN 7540-01-280-5500

Standard Form 298 (Rev. 2-89)
Prescribed by ANSI Std. Z39-18
298-102

Table of Contents

| | |
|-----------------------------------|----|
| Front cover | i |
| SF 298, Report Documentation page | ii |
| Annual Report | 1 |
| Conclusions | 2 |
| References | 2 |
| Appendices | 3 |

Parallel, Rapid Diffuse Optical Tomography of Breast

Introduction

The aim of this work is to develop and assess near infrared diffuse light imaging schemes for tumor detection and characterization using a combination of experimental, theoretical, and computational tools and techniques. During the last year we have experimentally investigated more rapid acquisition and computationally investigated the analysis of informationally dense diffuse optical data sets in the parallel plate compressed breast geometry.

Specific Aim 1: Parallel computing for 3D Reconstructions in the compressed breast geometry.

As we have reported in previous year, a parallel computer program to reconstruct the three-dimensional optical properties map of breast tissues in vivo has been developed and tested thoroughly with various tissue phantoms. However, the computer memory usage of the program was quite extensive, so the usage of all the available measured data was quite difficult.

As an alternative method, continuous-wave(CW) and frequency-domain(RF) version of TOAST (Time-resolved Optical Absorption and Scatter Tomography) by Simon Arridge et al. [1, 2] has been adapted for the parallel plane compressed breast geometry. TOAST uses 3D gradient-based nonlinear optimization scheme with Finite element forward solver. Its memory-efficient algorithm is suitable for dealing with informationally dense data set as ours. Under the collaboration with Arridge et al, the Finite element forward solver part has been parallized and tested. A novel scheme using a priori spectral information of the chromophores and scatteres [3] has been implemented into TOAST to fit for blood oxygen saturation and total hemoglobin concentration directly. The investigation of combining CW transmission and RF remission data in TOAST and optimizing the weighting of the measurements is in progress.

Specific Aim 2: Addition of CCD transmission to frequency domain compressed breast apparatus.

Addition of CCD transmission measurements to frequency domain compressed breast apparatus has been completed. We are currently investigating the advantage of adding white light source for CW measurements as well as adding more laser diodes which are sensitive to water and lipid spectra.

Specific Aim 3 : *Parallel Measurement and Image Reconstruction*

The characterization of the instruments and 3D reconstruction scheme has been reported [4]. The efficacy of newly improved reconstruction scheme is being tested for simulated data and previously constructed silicone tissue phantoms of various configuration and heterogeneities.

Significance :

We have shown that we could resolve the tumor-simulating phantom with reasonable resolution and accuracy using a hybrid instrument and 3D reconstruction algorithm[4]. This indicates the extrinsic contrast based breast imaging on human subjects can be achieved with similar degree of accuracy in detection and quantification of a tumor. We have started developing a method for the intrinsic contrast based breast imaging on phantom studies and on normal and high-risk subjects. The preliminary 3D reconstruction of the breast cancer shows high contrast in total hemoglobin concentration from the healthy breast tissue. The findings from normal subjects in terms of average optical properties and heterogeneities in normal breasts will help us distinguish the features due to tumors from those due to inter-patient variation, hormonal variation, or other physiological changes induced by the instrument design.

Conclusions

In our work over the last year we have developed and assessed the utility of various theoretical, experimental and computational near-infrared diffuse light imaging schemes for tumor detection and characterization within the human breast. We have theoretically and computationally investigated the application of parallel processing to 3-dimensional reconstruction in the compressed breast geometry. Significant progress was made in the implementation of a priori spectral information and RF data into the 3D image reconstruction scheme. We have recruited healthy subjects and high-risk patients to investigate the optical contrast of tumors. We are continuing to gather more clinical data to assess the efficacy of the developing instrumentation and algorithm development.

References

- [1] Arridge, S. R., Schweiger, M., Image reconstruction in optical tomography, Phil. Trans. Royal. Soc. B 352, 717-726 (1997).
- [2] Arridge, S. R., Schweiger, M., <http://www.medphys.ucl.ac.uk/~martins/toast/index.html>
- [3] Durduran, T., Choe, R., Culver, J. P., Zubkov, L., Holboke, M. J., Giammarco, J., Chance, B., Yodh, A. G., Bulk optical properties of healthy female breast tissue, Phys. Med. Biol. 47, 2847-2861 (2002)
- [4] Culver, J. P., Choe, R., Holboke, M. J., Zubkov, L., Durduran, T., Slemple, A., Ntziachristos, V., Chance, B., Yodh, A. G., Three-dimensional diffuse optical tomography in the parallel plane transmission geometry: Evaluation of a hybrid frequency domain/continuous wave clinical system for breast imaging, accepted to Medical Physics (2002)

Reportable Outcomes : presentations in the conference and publications

- Choe, R., Culver, J. P., Giammarco, J. M., Nayeem, A. I., Intes, X., Zubkov, L., Durduran, T., Holboke, M. J., Fraker, D., Chance, B., Yodh, A. G., 3D Hemoglobin Concentration and Oxygenation Image Reconstruction of Breast based on Intrinsic Contrast using RF/CW Hybrid System, ISOTT 2001 (Philadelphia, Aug. 2001)
- Choe, R., Durduran, T., Culver, J. P., Giammarco, J. M., Intes, X., Chance, B., Yodh, A. G., Bulk Optical Properties of Normal Breast with Endogeneous and Exogeneous Contrast, OSA Topicals (Miami, April 2002)
- Choe, R., Corlu, A., Culver, J. P., Durduran, T., Giammarco, J. M., Chance, B., Yodh, A. G., 3D diffuse optical tomography of healthy and tumor breasts in parallel plane geometry, GRC 2002, Lasers in Medicine and Biology
- Durduran, T., Choe, R., Culver, J. P., Zubkov, L., Holboke, M. J., Giammarco, J., Chance, B., Yodh, A. G., Bulk optical properties of healthy female breast tissue, Phys. Med. Biol. 47, 2847-2861 (2002)
- Culver, J. P., Choe, R., Holboke, M. J., Zubkov, L., Durduran, T., Slemper, A., Ntziachristos, V., Chance, B., Yodh, A. G., Three-dimensional diffuse optical tomography in the parallel plane transmission geometry: Evaluation of a hybrid frequency domain/continuous wave clinical system for breast imaging, accepted to Medical Physics (2002)

Personnel

- Arjun G. Yodh
- Turgut Durduran
- Re-Gine Choe
- Joseph Giammarco
- Britton Chance

Bulk optical properties of healthy female breast tissue

T Durduran¹, R Choe¹, J P Culver¹, L Zubkov¹, M J Holboke¹,
J Giammarco¹, B Chance² and A G Yodh¹

¹ Department of Physics and Astronomy, University of Pennsylvania, 209 S. 33rd Street,
Philadelphia, PA 19104, USA

² Department of Biochemistry and Biophysics, University of Pennsylvania, Philadelphia,
PA 19104, USA

E-mail: durduran@stwing.upenn.edu

Received 20 March 2002

Published 24 July 2002

Online at stacks.iop.org/PMB/47/2847

Abstract

We have measured the bulk optical properties of healthy female breast tissues *in vivo* in the parallel plate, transmission geometry. Fifty-two volunteers were measured. Blood volume and blood oxygen saturation were derived from the optical property data using a novel method that employed *a priori* spectral information to overcome limitations associated with simple homogeneous tissue models. The measurements provide an estimate of the variation of normal breast tissue optical properties in a fairly large population. The mean blood volume was $34 \pm 9 \mu\text{M}$ and the mean blood oxygen saturation was $68 \pm 8\%$. We also investigated the correlation of these optical properties with demographic factors such as body mass index (BMI) and age. We observed a weak correlation of blood volume and reduced scattering coefficient with BMI; correlation with age, however, was not evident within the statistical error of these experiments. The new information on healthy breast tissue provides insight about the potential contrasts available for diffuse optical tomography of breast tumours.

1. Introduction

Near-infrared (NIR) diffuse optical tomography (DOT) is emerging as a viable means for breast tumour detection and specification. This method relies on physiological factors such as blood volume (total haemoglobin concentration), blood oxygen saturation (ratio of oxy-haemoglobin to total haemoglobin concentration), water, lipid content and tissue scattering to enhance tumour specificity and sensitivity. Thus far, *in vitro* optical properties of breast have been reported (Cheong *et al* 1990, Peters *et al* 1990, Troy *et al* 1996, Bevilacqua *et al* 1997, Gayen and Alfano 1999), and pilot *in vivo* measurements of endogenous optical properties and endogenous tumour contrast

have been reported (Chance 1998, Kang *et al* 1993, Suzuki *et al* 1996, McBride *et al* 1999, Delpy and Cope 1997, Painchaud *et al* 1999, Tromberg *et al* 1997, Fishkin *et al* 1997, Cerussi *et al* 2001, 2002, Grosenick *et al* 1999, Franceschini *et al* 1997, Sickles 1984, Nioka *et al* 1994, Hoogeraad *et al* 1997, Ntziachristos *et al* 1998, 1999, 2000, Pogue *et al* 2001a, 2001b). The use of exogenous contrast agents has also been investigated (Gurfinkel *et al* 2000, Ntziachristos *et al* 1999, 2000, Ntziachristos and Chance 2001, Weissleder *et al* 1999, Hawrysz and Sevick-Muraca 2000, Mahmood *et al* 1999, Li *et al* 1985, O'Leary *et al* 1994, Sevick-Muraca and Burch 1994, Li *et al* 1996, Boas *et al* 1993). Indocyanine green (ICG) for example, was demonstrated to enhance breast tumour contrast *in vivo* (Gurfinkel *et al* 2000, Ntziachristos *et al* 1999, 2000, Ntziachristos and Chance 2001). Similar results were obtained with optically quenched near-infrared fluorescence dyes (Weissleder *et al* 1999, Hawrysz and Sevick-Muraca 2000, Mahmood *et al* 1999), suggesting that early detection of tumours may be possible. For a recent review of developments in optical methods in breast cancer diagnostics with emphasis on fluorescent contrast agents see Hawrysz and Sevick-Muraca (2000).

Diffuse optical tomography differs from its predecessor, diaphanography (Watmough 1982, Bartrum and Crow 1984, Alverdy *et al* 1990, Cutler 1929), because it employs a rigorous mathematical model for the propagation of photons in tissues. The diffusion model enables experimenters to separate tissue scattering effects from tissue absorption effects, and thus extract more quantitative information about tissue chromophores. The diffusion model can also be adapted to ameliorate a variety of complications that arise from tissue boundary (Fantini *et al* 1996), multi-layer effects (Franceschini *et al* 1999) and the heterogeneous structure of the tissue (Cubeddu *et al* 2000a). Finally the diffusion model provides a sound mathematical basis for data inversion and tomographic image reconstruction (Arridge and Hebden 1997).

This paper is concerned with the optical properties of healthy breast tissue. Since we are ultimately interested in differentiating diseased tissue from healthy tissue, it is desirable to measure and understand the properties of healthy tissues, including their variation with time and demographics. Thus far a few investigators have probed such changes with respect to hormone levels during the menstrual cycle (Cubeddu *et al* 2000b, 2000c), menopause (Suzuki *et al* 1996, Chance 1998, Cerussi *et al* 2001), age (Chance 1998, Tromberg *et al* 1997, Cerussi *et al* 2001, 2002, Cubeddu *et al* 1999, Suzuki *et al* 1996) and body mass index (BMI) (Pogue *et al* 2001a, Suzuki *et al* 1996, Cerussi *et al* 2002). Each of these investigations has particular strengths and weaknesses.

Suzuki *et al* (1996) studied the optical properties of 30 Japanese women. They employed a time-resolved optical system in the transmission geometry for measurement, but only a single wavelength and a single source-detector pair was employed. Nevertheless, they reported strong correlation of absorption and scattering properties with age, BMI and menstrual status; no correlation was observed with respect to breast thickness and pregnancy number. Cerussi *et al* (2001) recently published observations of 28 volunteers. These experiments improved on earlier measurements by using a multi-wavelength, multi-modulation-frequency optical system; however, the device utilized a single source-detector pair at relatively small separation and thus probed primarily within 1 cm of the tissue surface. Such tissue generally contains more fat. Their experiments revealed substantial changes in the breast tissue optical properties between pre- and post-menopausal women; some correlation between age and blood volume, water content and 'scatter power' were found, but the most important observation was that older breast tissues had different water and lipid content. A newer study using the same instrument (Cerussi *et al* 2002), with 30 volunteers further related their findings to BMI to verify the accuracy of the extracted lipid fraction and the relationship of the 'scatter power' to BMI. Cubeddu *et al* (2000b, 2000c) followed the tissue optical properties at multiple wavelengths

between 610–1010 nm throughout the menstrual cycle and quantified the changes for one volunteer. They reported changes with age, which could be attributed to tissue fat content (Cubeddu *et al* 1999). Finally, Pogue *et al* (2001a, 2001b) investigated 16 normal breasts using a cylindrical DOT system geared towards imaging. They found that blood volume was correlated with body mass index (BMI), but found no other strong correlations.

In this paper we present measurements of 52 healthy volunteers using our clinical diffuse optical imager in the compressed breast geometry. Informed consent was obtained from volunteers and the measurements were carried out over 18 months at the Hospital of University of Pennsylvania under local internal review board (IRB) approval. Our instrument was a prototype geared towards diffuse optical tomography in the parallel plate transmission geometry with soft compression. We used a single modulated source centrally located on one plate, and 153 detectors on the opposite plate. Measurements were performed at three wavelengths (830 nm, 786 nm, 750 nm). The modulation frequency was 140 MHz providing the phase and amplitude of 153 diffuse photon density waves (DPDWs) in transmission. Thus our measurements were sensitive to the bulk of the breast tissue (as opposed to near-surface tissues). For data analysis we employed a new scheme that utilized *a priori* information about the expected spectral dependence of scattering and absorption in a simple, infinite slab model; this 'physiologically constrained' approach substantially reduced inter-parameter cross-talk in our estimates of bulk optical properties. We directly obtain chromophore concentrations and scattering parameters as a result of these fits.

The haemoglobin concentrations thus obtained were used to calculate blood volume and blood oxygen saturation. Histograms of all properties provide new estimates of the range of healthy breast properties. The combination of blood volume and blood oxygen saturation information enables us to define ranges of tumour optical properties wherein substantial endogenous contrast should arise. The properties were related to age and body mass index (BMI); the latter exhibited some correlation with blood volume and with the reduced scattering coefficient. Physiological measurement noise was also estimated by repeated measurements of the same breast and by repeated measurements at a given detector position.

2. Instrumentation and clinical setting

Our optical breast imager is illustrated schematically in figure 1. We employ a parallel plate, transmission geometry with soft compression. The instrument uses three wavelengths—830 nm, 786 nm and 750 nm, and employs a scanning, fibre-coupled PMT detector (R928, Hamamatsu) for detection. The system is characterized by a noise equivalent power of $\approx 0.1 \text{ pW Hz}^{-1/2}$, a linearity in amplitude of 1%, and a phase drift of 0.25° over 80 dB. We calibrated the instrument over a broad range of input powers in order to extend this range. For transmission measurements the signal variation is typically $\approx 30 \text{ dB}$. In clinical measurements we utilize a single source position at the centre of the scanning region. The lasers are amplitude modulated at 140 MHz to produce diffuse photon density waves (DPDWs) in the medium. The amplitude and phase of the DPDW is recovered using a homodyne IQ-demodulation scheme (Yang *et al* 1997). Figure 1 shows a sketch of the electronics.

We have characterized the instrument with extensive phantom studies (Durduran *et al* 1999a, 1999b, 2000, 2001). More recently and as a result of our experience in pilot studies on volunteers, we have constructed a more complex imaging device in the same apparatus which combines RF and CW measurements (Culver *et al* 2000, 2002).

For the *in vivo* measurements the volunteer lies in the prone position. Her breast is inserted into a small tank filled with a near-matching solution of Intralipid and India-ink mixture (see figure 1). The detector is scanned along the output plate glass surface. The source is

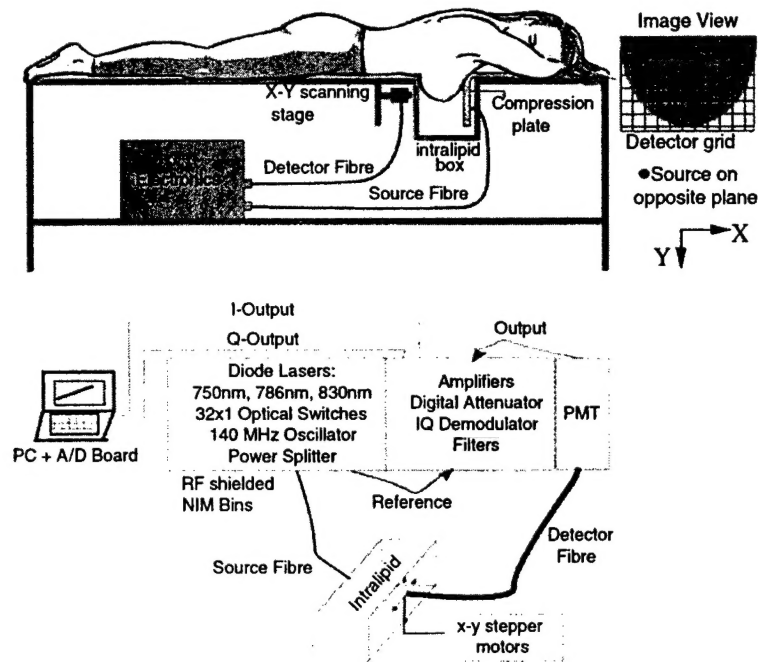


Figure 1. A sketch of the prototype clinical table. The volunteer lies in the prone position with her breast inserted into the tank through a large aperture on the bed. Soft compression is applied on the source plane and detector scans a 2D grid on the opposite plane. The image view shows the source detector positions as seen in the data. The lower inset shows the sketch of the system including the electronic components.

attached to the movable compression plate, which applies a gentle compression to the breast. The usual range of compression is 4.5 cm to 7 cm. It took ≈ 15 min to acquire data from a 9.6 cm (x) by 4.8 cm (y) scan region with 153 (17×9) measurement points. Feedback from volunteers was generally positive; compared to x-ray mammography, the soft-compression of the DOT instrument did not cause discomfort. We obtained two sets of data for each volunteer: (1) a measurement of the tank filled with Intralipid solution, without the breast, which allows us to normalize the instrument response for imaging purposes and to obtain an estimate of the breast tissue boundaries. (2) A measurement from the tank filled with Intralipid solution and the volunteer's breast. The Intralipid helps to reduce the detrimental effects of breast boundaries by acting as a matching medium. Measurements were repeated to assess physiological noise.

3. Theory and analysis

We modelled our parallel plate geometry as an infinite slab, bounded on one side by a glass window (the detector plane) and on the other by a white plate (the source plane). Previously (Durduran *et al* 1999a) we have shown that the chest wall affects the acquired data by effectively extending the diffusive medium above the tank; in practice this makes our infinite

slab approximation even better. Special care was taken during the data acquisition to centre the source and the detector grid on the breast tissue; however, occasionally some regions from outside the breast tissue were also in the field of view. In such cases we ignored grid points near the boundaries in our analyses. The solution for an infinite slab is obtained using image sources and is well known (Haskell *et al* 1994, Contini *et al* 1997, Martelli *et al* 1997).

For chromophore analysis, we employ a simple algorithm that utilizes *a priori* spectral information to reduce inter-parameter crosstalk (Durduran *et al* 2001). We outline this method below.

We decompose the absorption coefficient (μ_a) into contributions from different tissue chromophores, i.e.

$$\mu_a(\lambda) = \sum_i^{NC} \epsilon_i(\lambda) c_i. \quad (1)$$

Here the sum is over the different tissue chromophores and NC is the number of chromophores included in the sum. $\epsilon_i(\lambda)$ is the wavelength-dependent extinction coefficient of the i th chromophore (obtained from the literature (Prah 2001)³), and c_i is the concentration of the i th chromophore. The c_i are unknowns. Oxy- and deoxy-haemoglobin are the most significant chromophores in our spectral region. They can be combined to obtain blood volume (i.e. total haemoglobin concentration) and blood oxygen saturation. These quantities are important physiological tissue properties. For healthy breast tissue, the primary absorbers in our near infrared window are oxy- and deoxy-haemoglobin, lipid and water (Cerussi *et al* 2001). Because we used only a limited number of wavelengths, we introduced a relatively small, wavelength-dependent background absorption based on water and lipid signals measured by optical spectroscopy (Cerussi *et al* 2001). The water and lipid content of breast are taken to be 31% and 57%, respectively (White *et al* 1987, Woodard and White 1986, Lee *et al* 1997).

The other parameter characterizing the migration of photons through tissue is the reduced scattering coefficient (μ'_s). It has been shown that a simple Mie-scattering approximation is applicable to scattering from breast tissues (Cerussi *et al* 2001, Pogue *et al* 2001a, Cubeddu *et al* 1999, 2000b). Within this approximation we write μ'_s as (Mourant *et al* 1997, Nilsson *et al* 1998)

$$\mu'_s(\lambda) = ax^b\lambda^{-b} \quad (2)$$

where a , b are free parameters. a is proportional to the density of the scattering centres and b depends on their size. $x = 2\pi rn_m$ where n_m is the index of refraction of the medium and r is the homogeneous sphere radius for a 'typical scatterer'. For breast tissue with a distribution of different size scatterers, we define a 'Mie-equivalent radius' ($r = r_e$) as an 'average' scatterer size (Nilsson *et al* 1998), and use a simplified version of equation (2), which has been shown to be a reasonably good approximation over the wavelength range we employ, and wherein the x dependence is lumped into the coefficient A :

$$\mu'_s(\lambda) = A\lambda^{-b}. \quad (3)$$

Cerussi *et al* (2001) have found empirically that b (called the 'scatter power') is a good indicator of changes in breast tissue physiology with age. Our fitted values of the scattering parameters a and b are not very precisely obtained as a result of the limited number of wavelengths used in our study, e.g. b was measured to be 1.27 ± 0.82 .

We formulate the inversion problem in terms of the variables described above assuming an infinite slab model. Traditionally μ_a and μ'_s are reconstructed for each wavelength separately.

³ We kindly thank S J Matcher for providing the spectra for lipids.

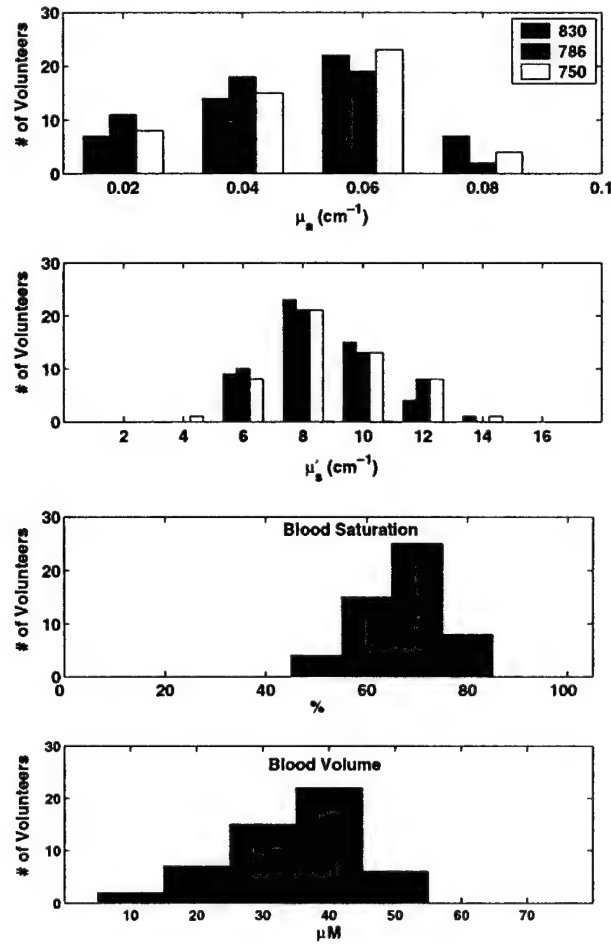


Figure 2. Starting from the top, shown are μ_a , μ_s' , blood oxygen saturation and blood volume histograms.

However, due to model mismatch, and experimental and physiological noise, significant inter-parameter cross-talk is introduced by the standard procedure, often leading to large errors in blood volume and saturation. Instead, we directly reconstruct the concentrations (c_i), A , and b . This procedure constrains the fitting algorithm using *a priori* spectral information. Thus we globally analyse the whole set of data, instead of analysing each wavelength independently and then combining the results. This approach substantially reduces the inter-parameter cross-talk (Durduran *et al* 2001).

In the calculation we minimize $\chi^2 = \sum |\Phi_m - \Phi_c|^2$ where Φ_m is the measured fluence and Φ_c is the calculated fluence. The sum is over the source detector pairs and all wavelengths. We use the Nelder–Mead simplex (direct search) method implemented in MATLAB function 'fminsearch' to fit for the unknowns by minimizing χ^2 . We then calculate blood oxygen saturation and blood volume from the relevant haemoglobin concentrations.

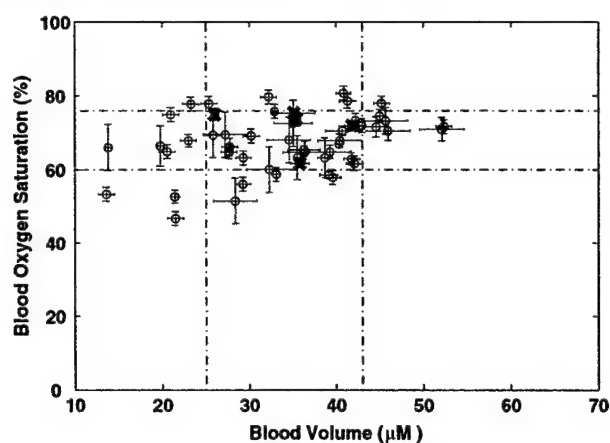


Figure 3. Blood oxygen saturation versus blood volume with the dashed lines indicating the ranges for normal tissue from the mean and standard deviation of the healthy breast tissue. Crosses (×) indicate menopausal volunteers.

Table 1. Average optical properties, physiological parameters and standard deviation from the histograms.

| | | | |
|------------------------------|-------------------|-------------------|-------------------|
| λ (nm) | 830 | 786 | 750 |
| μ_a (cm ⁻¹) | 0.046 ± 0.027 | 0.041 ± 0.025 | 0.046 ± 0.024 |
| μ'_s (cm ⁻¹) | 8.3 ± 2.0 | 8.5 ± 2.1 | 8.7 ± 2.2 |
| Blood volume (μM) | 34 ± 9 | | |
| Blood oxygen saturation (%) | 68 ± 8 | | |

4. Results and discussion

4.1. Optical properties of healthy breast tissue

In order to establish a range of optical and physiological properties for the healthy breast tissue we made histograms of the fitted properties. The results are summarized in figure 2. The values lie within the expected physiological range. Mean and standard deviation are shown in table 1.

Some researchers have speculated that tumours and other diseased tissue are distinguished from normal tissues by the relative value of their blood volume and blood oxygen saturation. For example, malignant tumours might be expected to have high blood volume with a low oxygen saturation since both a higher blood content and higher metabolism are necessary to achieve tumour growth in proliferating tumour tissue (Thomsen and Tatman 1998). Figure 3 shows blood oxygen saturation plotted versus blood volume for each breast (crosses (×) indicate menopausal volunteers). The dashed lines indicate the measured range of blood volume and blood oxygen saturation for normal breasts from table 1 (i.e. the mean and standard deviation). The error bars for each individual are obtained from the standard deviation of repeated measurements of the same breast. In order to employ endogeneous contrast effectively in breast DOT, tumour tissue properties should ideally lie in one of the 'other' regions defined on this plot.

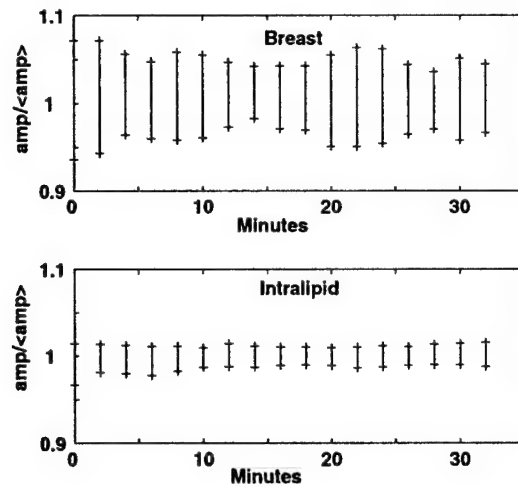


Figure 4. Normalized amplitude measured on breast and Intralipid sample by visiting the same 17 points every two minutes ten times.

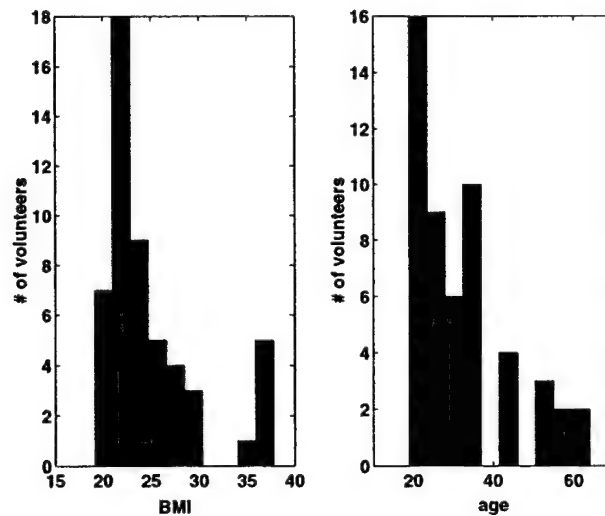


Figure 5. Distribution of patients in terms of their body mass index (BMI) (left) and age (right).

4.2. Physiological noise

Apart from characterizable noise due to electronics, optics and positioning of the sources and detectors, there is additional noise in the measurements as a result of changes in the physiological state of the tissue during the measurements. Respiration, movement, heart beat and blood flow downstream of the hanging breast are some factors that contribute to this 'physiological noise'.

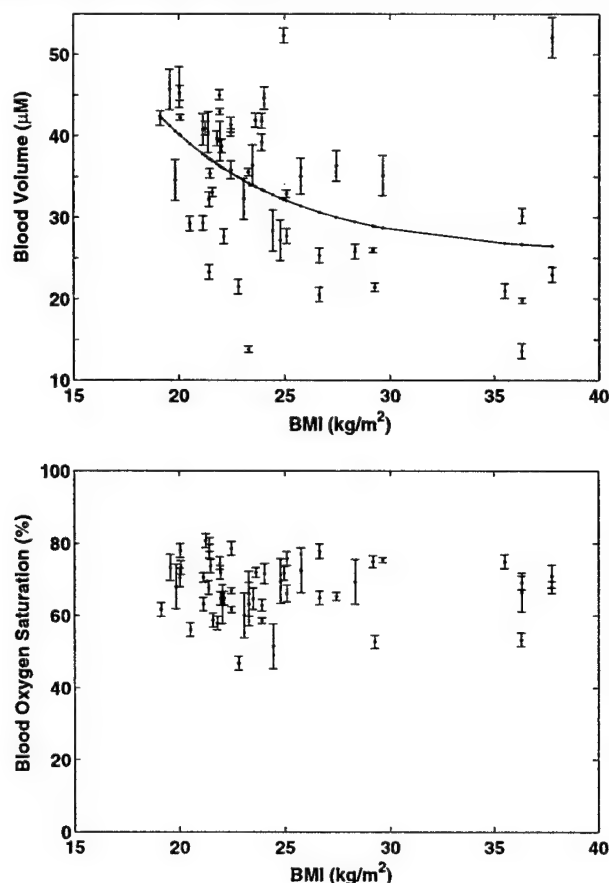


Figure 6. Top: blood volume versus BMI with a decaying exponential fit (correlation coefficient 0.42); bottom: blood oxygen saturation (correlation coefficient 0.03) versus BMI.

In order to estimate this effect, the scanning detector was modified to repeat each of the 17 source–detector combinations ten times every two minutes. The main results are shown in figure 4 where we plot the time series of normalized amplitude (phase is not shown) obtained from measurements on an Intralipid sample and on breast tissue. The signals from the Intralipid are stable to within 1–2%, whereas the breast tissue has dispersions of 5–10%. This provides us with an estimate of the physiological noise in our experiments.

We also performed repeated measurements of the same breast with minimal movement of the breast. By comparing repeated measurements, we find that the average standard deviation is 11% for μ_a , 4% for μ'_s , 4% for blood oxygen saturation and 5% for blood volume (see, for example, error bars in figure 3). These values are consistent with the variations in the amplitude and phase observed in figure 4.

4.3. Demographics and optical properties

As mentioned above, it might be expected that optical properties would show a variation with demographics. We investigated the correlation of our results with two demographic quantities:

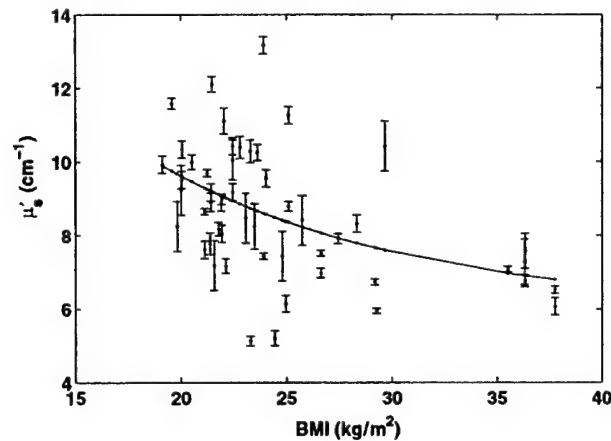


Figure 7. μ'_s at 830 nm versus BMI with a decaying exponential fit. Other wavelengths show similar trends. The correlation coefficient is 0.46.

body mass index (BMI) and age, whose distributions are shown in figure 5. The mean (standard deviation) age of the volunteer population lies in the radiographically dense population and it is 32 ± 12 years. The mean (standard deviation) BMI is 25 ± 5 . Only five patients were menopausal and one patient was peri-menopausal. Our study was not originally aimed towards establishing correlations with demographic factors and future studies will be further optimized for looking specifically at those aspects of the problem. Specifically, we have used only three wavelengths and assumed flat water and lipid concentration in our analysis. This limits our spectral information which further limits the quality of these correlations (Cerussi *et al* 2002). Further spatial information would also be valuable in distinguishing different regions of the breast tissue. With these caveats, we now outline our findings and compare them to the results available in the literature from other studies. Pogue *et al* (2001a) used a similar system geared towards imaging and reported that blood volume had a correlation with body mass index (BMI) which relates the weight and height of an individual. They did not report strong correlation between any other quantities and BMI or age. Cerussi *et al* (2001) reported weak correlation between blood volume and scatter power (b) with age and measured changes of lipid concentration with age and BMI (Cerussi *et al* 2002).

Our findings are shown in figure 6 for correlations with BMI. Our observed correlation of blood volume to BMI is similar to reports by Pogue *et al* (2001a). A higher BMI indicates more tissue fat content. In compositional studies, a higher fat content correlates with a lower blood content (Thomsen and Tatman 1998, Duck 1990, White *et al* 1987, Woodard and White 1986, Gertig *et al* 1999, Lee *et al* 1997). The correlation coefficient is significantly higher for blood volume than for blood oxygen saturation (0.42 versus 0.03).

We also observed a similar correlation of BMI and μ'_s as shown in figure 7. Cerussi *et al* (Cerussi *et al* 2001, 2002) showed that the scattering power and μ'_s change with the fat content. BMI is a measure of the tissue fat content, hence the present result is in qualitative agreement with their observations.

Figure 8 shows the correlation of the blood volume and blood oxygen saturation with age. Our results again indicate an agreement with Pogue *et al* (2001a); we do not see any

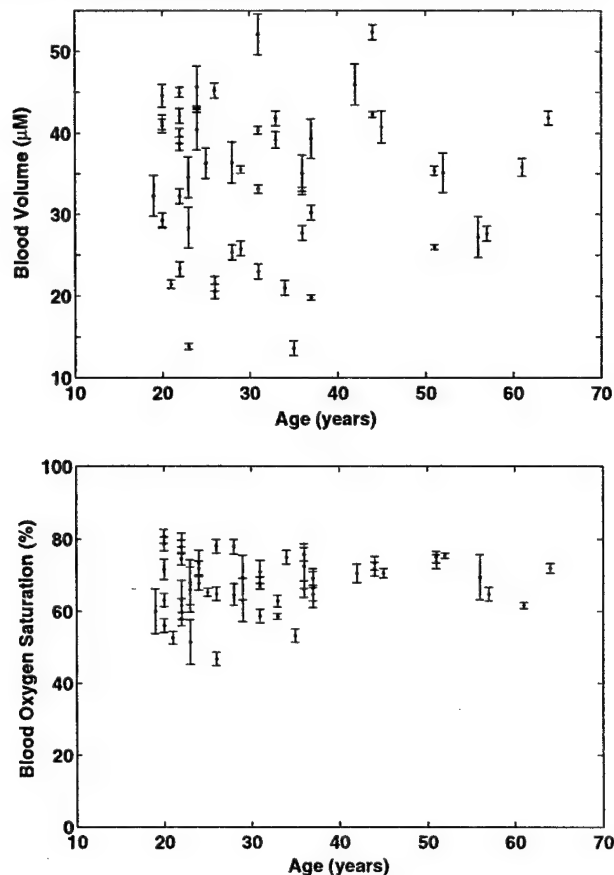


Figure 8. Top: blood volume versus age. The correlation coefficient is 0.0292. Bottom: blood oxygen saturation versus age. The correlation coefficient is 0.15.

clear correlations within our current signal-to-noise. As shown in figure 9 we do not see a correlation of μ'_s with age as well.

Our study had a different sensitivity to that of Cerussi *et al* (2001, 2002) who showed that there is considerable change in breast properties with age. Their main observation is that older breast tissue has a different water and lipid content, which in turn affects the scattering and absorption properties of the tissue. We suspect their instrument was particularly sensitive to this aspect because it measured mainly the outer ≈ 1 cm of the tissue and had many wavelengths which allowed more accurate derivation of the wavelength dependence of the scattering. Our results, by contrast, sample a larger volume in transmission geometry. Therefore, we sample the fatty tissue as well as the nodules and vasculature extensively. There are expected changes in the breast tissue structure with age throughout the total volume, however, our study was not sensitive to those changes as it did not attempt to distinguish different regions of the breast tissue. We are not sensitive to lipid content because of our limited spectral information and because of our assumptions regarding the lipid and water content of the breast. The latter

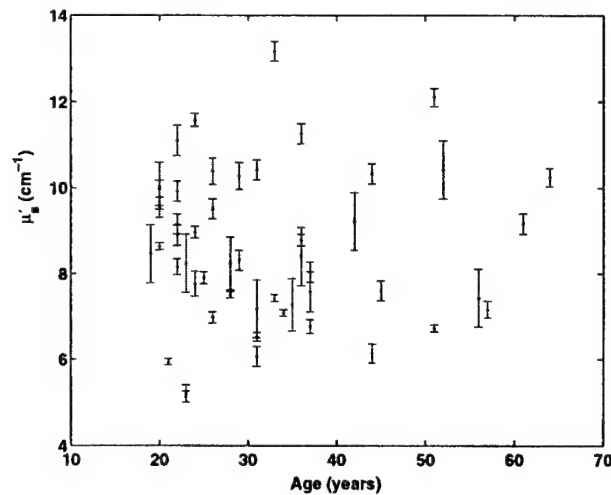


Figure 9. μ'_s at 830 nm versus age. Other wavelengths show similar trends. The correlation coefficient is 0.02.

was shown to introduce errors in an analysis by Cerussi *et al* (2002). This fact, of course, points further to the need for diffuse optical imaging with extensive spectral information. Our results are important, because they establish baseline optical properties in the transmission plate geometry, and most imaging systems rely on sampling a large volume of the breast tissue. Indeed it has previously been reported that differences in acquisition geometry can induce changes in bulk properties (Cubeddu *et al* 2000b, 2000a).

5. Conclusion

The bulk optical properties of healthy female breast tissue were measured *in vivo* in a parallel plate, with transmission geometry geared towards diffuse optical tomography. Fifty-two volunteers with healthy breasts were measured. The analysis was done with a novel method which employs *a priori* spectral knowledge to overcome the shortcomings of simplified models of the heterogeneous breast tissue. Our results establish a range for the healthy breast properties in this geometry over a fairly large population. The blood volume was $34 \pm 9 \mu\text{M}$ and blood oxygen saturation was $68 \pm 8\%$ (see table 1). We investigated the correlation of optical properties with demographic properties and observe a weak correlation of blood volume and reduced scattering coefficient with body mass index.

Acknowledgments

This work was supported by NIH 2-RO1-CA-75124-04, Army DAMD17-00-1-0408 grants. We gratefully acknowledge useful discussions with D N Pattanayak, C Cheung, X Intes, J Ripoll, B W Pogue and B J Tromberg who provided useful insights into acquisition and analysis of these datasets. We also thank L Pfaff, C Cowan and K Thrush for their help in clinical measurements and, Y K Choe for his help in illustrations.

References

- Alverdy A, Andersson I and Aspegren K 1990 Light scanning versus mammography for the detection of breast cancer in screening and clinical practice: a Swedish multicenter study *Cancer* **65** 1671-77
- Arridge S R and Hebden J C 1997 Optical imaging in medicine: II. Modelling and reconstruction *Phys. Med. Biol.* **42** 841-54
- Bartrum R J and Crow H C 1984 Transillumination light scanning to diagnose breast cancer: a feasibility study *Am. J. Roentgen.* **142** 409-14
- Bevilacqua F, Marquet P, Coquoz O and Depeursinge C 1997 Role of tissue structure in photon migration through breast tissues *Appl. Opt.* **36** 44-48
- Boas D A, O'Leary M A, Chance B and Yodh A G 1993 Scattering and wavelength transduction of diffuse photon density waves *Phys. Rev. E* **47** 2999-3002
- Cerussi A E, Berger A J, Bevilacqua F, Shah N, Jakubowski D, Butler J, Holcombe R F and Tromberg B J 2001 Sources of absorption and scattering contrast for near-infrared optical mammography *Acad. Radiology* **8** 211-18
- Cerussi A E, Jakubowski D, Shah N, Bevilacqua F, Lanning R, Berger A J, Hsiang D, Butler J, Holcombe R F and Tromberg B J 2002 Spectroscopy enhances the information content of optical mammography *J. Biomed. Opt.* **7** 60-71
- Chance B 1998 Near-infrared images using continuous, phase-modulated, and pulsed light with quantitation of blood and blood oxygenation *Adv. Opt. Biop. and Opt. Mammography, Ann. of New York Acad. of Sci.* **838** 19-45
- Cheong W F, Prah S A and Welch A J 1990 A review of the optical properties of biological tissues *IEEE J. Quantum Electron.* **26** 2166-85
- Contini D, Martelli F and Zaccanti G 1997 Photon migration through a turbid slab described by a model based on diffusion approximation: I. Theory *Appl. Opt.* **36** 4587-99
- Cubeddu R, D'Andrea C, Pifferi A, Taroni P, Torricelli A and Valentini G 2000a Spatial changes in the absorption spectrum of the female breast *Optical Society of America Biomedical Topicals Meeting (Miami, FL)* pp 419-21
- Cubeddu R, D'Andrea C, Pifferi A, Taroni P, Torricelli A and Valentini G 2000b Effects of the menstrual cycle on the red and near-infrared optical properties of the human breast *Photochem. Photobiol.* **72-73** 383-91
- Cubeddu R, D'Andrea C, Pifferi A, Taroni P, Torricelli A and Valentini G 2000c Effects of the menstrual cycle on the red and near-infrared optical properties of the human breast *Optical Society of America Biomedical Topicals Meeting (Miami, FL)* pp 323-25
- Cubeddu R, Pifferi A, Taroni P, Torricelli A and Valentini G 1999 Noninvasive absorption and scattering spectroscopy of bulk diffusive media: an application to the optical characterization of human breast *Appl. Phys. Lett.* **74-76** 874-6
- Culver J P, Choe R, Holboke M J, Zubkov L, Durduran T, Slemp A, Ntziachristos V, Chance B and Yodh A G 2002 Three-dimensional diffuse optical tomography in the parallel plane transmission geometry: evaluation of a hybrid frequency domain/continuous wave clinical system for breast imaging *Med. Phys.* at press
- Culver J P, Ntziachristos V, Zubkov L, Durduran T, Pattanayak D N and Yodh A G 2000 Data set size and image quality in diffuse optical mammography: evaluation of a clinical proto type *Optical Society of America Biomedical Topicals Meeting (Miami, FL)* pp 392-94
- Cutler M 1929 Transillumination as an aid in the diagnosis of breast lesions *Surgery, Gynecol. Obstet.* **48** 721
- Delpy D T and Cope M 1997 Quantification in tissue near-infrared spectroscopy *Philos. Trans. R. Soc. Lond. B: Biol. Sci.* **352** 649-59
- Duck F A 1990 *Physical Properties of Tissue* (New York: Academic) pp 320-28
- Durduran T, Culver J P, Zubkov L, Choe R, Holboke M J, Chance B and Yodh A G 2001a Bulk optical properties of normal female breasts measured with a frequency domain clinical imager *Photonics West 2001, SPIE* vol 4250-65
- Durduran T, Culver J P, Zubkov L, Choe R, Holboke M, Pattanayak D N, Chance B and Yodh A G 1999a Bulk optical properties of normal breasts and tissue phantoms obtained with clinical optical imager *Proc. Inter-Institute Workshop on In Vivo Optical Imaging at the NIH (Bethesda, MD)* ed A H Gandjbakhche, pp 130-35
- Durduran T, Culver J P, Zubkov L, Choe R, Holboke M J, Pattanayak D N, Chance B and Yodh A G 2000 Bulk optical properties of normal breasts and tissue phantoms obtained with clinical optical imager *Optical Society of America Biomedical Topicals Meeting (Miami, FL)* pp 386-8
- Durduran T, Culver J P, Zubkov L, Holboke M J, Choe R, Li X D, Chance B, Pattanayak D N and Yodh A G 1999b Diffraction tomography in diffuse optical imaging; filters and noise *Photonics West 1999, SPIE* vol 3597-101 (San Jose, CA: SPIE)

- Durduran T, Giammarco J, Culver J P, Choe R, Zubkov L, Holboke M J, Yodh A G and Chance B 2001b Explicit inclusion of chromophore absorption and scattering spectra for diffuse optical imaging and spectroscopy *Photonics West 2001, SPIE* vol 4250–85
- Fantini S, Franceschini M A, Gaida G, Gratton E, Jess H and Mantulin W W 1996 Frequency-domain optical mammography: edge effect corrections *Med. Phys.* **23** 149–57
- Fishkin J B, Coquoz O, Anderson E R, Brenner M and Tromberg B J 1997 Frequency-domain photon migration measurements of normal and malignant tissue optical properties in a human subject *Appl. Opt.* **36** 10–20
- Franceschini M A, Gratton E, Hueber D and Fantini S 1999 Near-infrared absorption and scattering spectra of tissues *in vivo Proc. SPIE* **3597** 526–31
- Franceschini M A, Moesta K T, Fantini S, Gaida G, Gratton E, Jess H, Seeber M, Schlag P M and Kashke M 1997 Frequency-domain techniques enhance optical mammography: initial clinical results *Proc. of Nat. Ac. of Sci* **94** 6468–73
- Gayen S K and Alfano R R 1999 Sensing lesions in tissues with light *Opt. Exp.* **4** 475–80 (webpage <http://epubs.osa.org/oearchive/source/9627.htm>)
- Gertig D M, Stillmann I E, Byrne C, Spiegelman D, Schnitt S J, Connolly J L, Colditz G A and Hunter D J 1999 Association of age and reproductive factors with benign breast tissue composition *Cancer Epidemiol. Biostat. Prev.* **8** 873–9
- Grosenick D, Wabnitz H, Rinneberg H H, Moesta K T and Schlag P M 1999 Development of a time-domain optical mammograph and first *in vivo* applications *Appl. Opt.* **38** 2927–43
- Gurfinkel M *et al* 2000 Pharmacokinetics of ICG and HPPH-car for the detection of normal and tumour tissue using fluorescence, near-infrared reflectance imaging: a case study *Photochem. Photobiol.* **72** 94–102
- Haskell R C, Svaasand L O, Tsay T, Feng T, McAddams M S and Tromberg B J 1994 Boundary Conditions for the diffusion equation in radiative transfer *J. Opt. Soc. Am. A* **11** 2727–41
- Hawrysz D J and Sevcik-Muraca E 2000 Developments toward diagnostic breast cancer imaging using near-infrared optical measurements and fluorescent contrast agents *Neoplasia* **2** 388–417
- Hoogeraad J H, van der Mark M B, Colak S B, Hooft G W and van der Linden E S 1997 First results from the Philips optical mammoscope *Photon Propagation of tissues III* vol 3194, ed D A Benaron, B Chance and M Ferrari (SPIE) pp 184–90
- Kang K A, Chance B, Zhao S, Srinivasan S, Patterson E and Trouping R 1993 Breast tumour characterization using near-infrared spectroscopy *Photon Migration and Imaging in Random Media and Tissues* vol 1888, ed R R Alfano and B Chance (Bellingham, WA: SPIE) pp 487–99
- Lee N A, Rusinek H, Weinreb J C, Chandra R, Singer R C and Newstead G M 1997 Fatty and fibroglandular tissue volumes in the breasts of women 20–83 years old: comparison of x-ray mammography and computer-assisted MR imaging *Am. J. Radiol.* **168** 501–06
- Li X D, Beauvoit B, White R, Nioka S, Chance B and Yodh A G 1985 Tumour localization using fluorescence of indocyanine green (ICG) in rat model *Proc. SPIE* **2389** 789
- Li X D, O'Leary M A, Boas D A, Chance B and Yodh A G 1996 Fluorescent diffuse photon-density waves in homogeneous and heterogeneous turbid media—analytic solutions and applications *Appl. Opt.* **35** 3746–58
- Mahmood U, Tung C H, Bogdanov A and Weissleder R 1999 Near-infrared optical imaging of protease activity for tumour detection *Radiology* **213** 866–70
- Martelli F, Contini D, Taddeucci A and Zaccanti G 1997 Photon migration through a turbid slab described by a model based on diffusion approximation: II. Comparison with Monte Carlo results *Appl. Opt.* **36** 4600–12
- McBride T O, Pogue B W, Gerety E D, Poplack S B, Osterberg U L and Paulsen K D 1999 Spectroscopic diffuse optical tomography for the quantitative assessment of hemoglobin concentration and oxygen saturation in breast tissue *Appl. Opt.* **38** 5480–90
- Mourant J R, Fuselier T, Boyer J, Johnson T M and Bigio I J 1997 Predictions and measurements of scattering and absorption over broad wavelength ranges in tissue phantoms *Appl. Opt.* **36** 949–57
- Nilsson A M, Stureson K C, Liu D L and Andersson-Engels S 1998 Changes in spectral shape of tissue optical properties in conjunction with laser-induced thermotherapy *Appl. Opt.* **37** 1256–67
- Nioka S, Miwa M, Orel S, Schnall M, Haida M, Zhao S and Chance B 1994 Optical imaging of human breast cancer *Adv. Exp. Med. Biol.* **361** 171–9
- Ntziachristos V and Chance B 2001 Probing physiology and molecular function using optical imaging: applications to breast cancer *Breast Cancer Res.* **3** 41–7
- Ntziachristos V, Ma X H and Chance B 1998 Time-correlated single photon counting imager for simultaneous magnetic resonance and near-infrared mammography *Rev. Sci. Instrum.* **69** 4221–33
- Ntziachristos V, Yodh A G, Schnall M and Chance B 1999 Comparison between intrinsic and extrinsic contrast for malignancy detection using NIR mammography *Proc. Optical Tomography and Spectroscopy of Tissue III* vol 3597, ed B Chance, R R Alfano and B J Tromberg (San Jose, CA: SPIE) pp 565–70

- Ntziachristos V, Yodh A G, Schnall M and Chance B 2000 Concurrent MRI and diffuse optical tomography of breast after indocyanine green enhancement *Proc. Nat. Acad. Sci. USA* **97** 2767–72
- O'Leary M A, Boas D A, Chance B and Yodh A G 1994 Reradiation and imaging of diffuse photon density waves using fluorescent inhomogeneities *J. Luminesc.* **60** 281–68
- Painchaud Y, Mailloux A, Harvey E, Verreault S, Frechette J, Gilbert C, Vernon M L and Beaudry P 1999 Multi-port time-domain laser mammography: results on solid phantom and volunteers *Int. Symp. Biomedical Optics* vol 3597 (Proc. SPIE) pp 548–55
- Peters V G, Wyman D R, Patterson M S and Frank G L 1990 Optical properties of normal and diseased human breast tissues in the visible and near infrared *Phys. Med. Biol.* **35** 1317–34
- Pogue B W, Poplack S D, McBride T O, Jiang S, Osterberg U L and Paulsen K D 2001a Near-infrared tomography: status of Dartmouth imaging studies and future directions (webpage <http://www.dartmouth.edu/~biolaser/>)
- Pogue B W, Poplack S P, McBride T O, Wells W A, Osterman K S, Osterberg U L and Paulsen K D 2001b Quantitative hemoglobin tomography with diffuse near infrared spectroscopy: pilot results in the breast *Radiology* **218** 261–6
- Prahl Scott 2001 Optical properties spectra (webpage <http://omlc.ogi.edu/spectra/index.html>)
- Sevick-Muraca E and Burch C L 1994 Origin of phosphorescence signals re-emitted from tissues *Opt. Lett.* **19** 1928–30
- Sickles E A 1984 Breast cancer detection with transillumination and mammography *Am. J. Roentgen.* **142** 841–4
- Suzuki K, Yamashita Y, Ohta K, Kaneko M, Yoshida M and Chance B 1996 Quantitative measurement of optical parameters in normal breasts using time-resolved spectroscopy: *in vivo* results of 30 Japanese women *J. Biomed. Opt.* **1** 330–4
- Thomsen S and Tatman D 1998 Physiological and pathological factors of human breast disease that can influence optical diagnosis *Adv. Opt. Biop. Opt. Mammography, Ann. N. Y. Acad. Sci.* **838** 171–93
- Tromberg B J, Coquoz O, Fishkin J, Pham T, Anderson E R, Butler J, Cahn M, Gross J D, Venugopalan V and Pham D 1997 Non-invasive measurements of breast tissue optical properties using frequency-domain photon migration *Philos. Trans. R. Soc. Lond. B: Biol. Sci.* **352** 661–8
- Troy T L, Page D L and Sevick-Muraca E 1996 Optical properties of normal and diseased breast tissue: prognosis for optical mammography *J. Biomed. Opt.* **1** 342–55
- Watmough D J 1982 Transillumination of breast tissues: factors governing optimal imaging of lesions *Radiology* **147** 89–92
- Weissleder R, Tung C H, Mahmood U and Bogdanov A 1999 *In vivo* imaging with protease-activated near-infrared fluorescent probes *Nat. Biotech.* **17** 375–8
- White D R, Woodard H Q and Hammond S M 1987 Average soft-tissue and bone models for use in radiation dosimetry *Br. J. Radiol.* **60** 907–13
- Woodard H Q and White D R 1986 The composition of body tissues *Br. J. Radiol.* **59** 1209–19
- Yang Y, Liu H, Li X and Chance B 1997 Low-cost frequency-domain photon migration instrument for tissue spectroscopy, oximetry and imaging *Opt. Eng.* **36** 1562–69

Three-dimensional diffuse optical tomography in the parallel plane transmission geometry: Evaluation of a hybrid frequency domain/continuous wave clinical system for breast imaging.

Joseph P. Culver^{†‡}, Regine Choe[†], Monica J. Holboke[†], L. Zubkov[†], T. Durduran[†], A. Slemp[†], V. Ntziachristos[‡], B. Chance[‡], A. G. Yodh[†]

[†]*Department of Physics and Astronomy University of Pennsylvania Philadelphia, PA, 19104-6396*

[‡]*Department of Biophysics and Biochemistry, University of Pennsylvania Philadelphia, PA, 19104-6396*

(March 8, 2002)

Abstract

Three-dimensional diffuse optical tomography(DOT) of breast requires large data sets for even modest resolution (1 cm). We present a hybrid DOT system that combines a limited number of frequency domain (FD) measurements with a large set of continuous wave (CW) measurements. The FD measurements are used to quantitatively determine tissue averaged absorption and scattering coefficients. The larger CW data sets (10^5 measurements) collected with a lens coupled CCD, permit 3D DOT reconstructions of a 1-liter tissue volume. To address the computational complexity of large data sets and 3D volumes we employ finite difference based reconstructions computed in parallel. Tissue phantom measurements evaluate imaging performance. The tests include: point spread function measures of resolution, characterization of the size and

[†]To whom correspondence should be addressed (jculver@nmr.mgh.harvard.edu)

contrast of single objects, field of view measurements and spectral characterization of constituent concentrations. We also report *in vivo* measurements. Average tissue optical properties of healthy breast are used to deduce oxy- and deoxy-hemoglobin concentrations. Differential imaging with a tumor phantom adhered to the surface of a healthy breast demonstrate 3D imaging in the presence of physiologic fluctuations. This tomography system provides robust, quantitative, full 3D image reconstructions with the advantages of high data throughput, single detector-tissue coupling path, and large (1L) imaging domains. In addition, we find that point spread function measurements provide a useful and comprehensive representation of system performance.

Keywords: optical tomography, NIR spectroscopy, breast imaging, clinical system

I. INTRODUCTION

Diffuse optical tomography (DOT) enables researchers to translate highly scattered, light signals into clinically meaningful information about human tissue¹⁻⁵. The tomographic approaches are new and offer substantially improved characterization of lesions compared to transillumination approaches of the past⁶⁻⁸. Intrinsic contrast derived from oxy- and deoxy-hemoglobin have been used to differentiate tumors from normal tissue based on vascular signatures^{3,9,10}. Extrinsic contrast, for example with existing vascular based agents such as indocyanine green, have exhibited significant tumor contrast enhancement^{5,11}. Ultimately, perhaps the most promising optical imaging schemes, may involve targeted agents to select cancer tissue based on peptide and molecular level bindings¹². The exquisite sensitivity of optical spectroscopy to both intrinsic and extrinsic agents make DOT attractive. However, before clinically optimized optical 3D imaging systems can be realized, several challenges remain to be solved.

The main experimental challenges for DOT relate to the speed and size of the collected data set. Coverage and resolution demand large data sets. Patient movement and physiologic fluctuations necessitate fast collection speeds. In fact, full coverage tomography of breast requires large data sets for even modest spatial resolution (e.g. $\approx 1\text{cm}$). Consider a DOT system that aims to provide 2-10 mm resolution in deep breast tissue (i.e. depths of 1 to 4 cm) with 1 Liter volume coverage. Even if we naively assume that a measurement number equal to the number of voxels is sufficient, we require from 10^3 (1 cm resolution) to 10^5 (2 mm resolution) measurements. Furthermore there is often an advantage to oversampling for signal averaging considerations, or for handling surface features that have sub millimeter structure and are near the regions of high measurement sensitivity¹³. Most clinical prototypes used for *in vivo* measurements have had much smaller data sets, in the range of 10^1 to 10^3 optode pairings^{3,5}, though recently a few systems with larger data sets have been reported². In this paper we present the results of a comprehensive investigation on the design, optimization and imaging performance of a hybrid DOT system that combines

a limited number of frequency domain measurements (720) with a significantly larger set of CW measurements (10^5). Before discussing the design in detail we briefly review our design rationale.

Every diffuse optical tomography system must make compromises about data type and number, measurement geometry, optode placement, and reconstruction method. Generally for absorption and scattering images there are three possible measurement approaches; time domain (pulsed input light with pulse duration $\tau_p \approx 100$ ps), frequency domain (modulated input light with frequency $\omega \approx 10^6 - 10^9$ Hz), continuous-wave ($\omega \approx DC - 100$ kHz). The time domain approach yields the most information per optode pair when the signal-to-noise ratio is sufficiently large, but it is usually the most expensive technique per optode pair. Continuous-wave (cw) measurements on the other hand are the least expensive and yield the least information per optode pair. Within the diffusion approximation the tissue is described by space- and time- dependent absorption and scattering coefficients and index of refraction¹⁴. To extract and separate variables at a single light wavelength a system needs at least three independent measures¹⁵ (for example multiple frequency domain or a time domain measurements). On a per-optode basis the frequency-domain and time-resolved measurements would seem to have an advantage over the CW approach. However, in practice it is possible to reduce the number of time-independent measurements needed by making assumptions about the medium such as its absorption and scattering properties. Imaging of differential changes can also dramatically improve the robustness of reconstruction¹⁶.

The most popular geometry for breast imaging has been the 2D circular array of sources and detectors¹⁷⁻²¹. This geometry is appealing, in part because of its similarity to the geometries used for computer aided tomography. It benefits from a full 2D measurement view over the entire circumference of the tissue volume. Full exploitation of this geometry requires large dynamic range and large channel separation so that the high light intensities at the close distances do not contaminate the low light levels (10^{-6} lower) at the long source detector separations. Another attractive geometry, which builds on experience with conventional mammography is the planar geometry which has been employed in both par-

allel scanning modes^{9,22} and limited view DOT arrangements^{5,23}. The disadvantage of this geometry is that the view is limited. It does not fully surround the surface of the tissue volume. An advantage is that the tissue is compressed providing increased light transmission and increased resolution, since resolution performance falls off with distance from the measurement surface^{13,23-25}. In addition, in the parallel plate transmission mode the dynamic range requirements of the detection system are reduced, and the mechanics of adapting to different breast sizes is reduced to a simple planar translation analogous to traditional X-ray mammography.

With these considerations in mind, we have pursued a hybrid frequency domain/continuous wave approach with massively parallel detection via a lens coupled CCD camera. The frequency domain (FD) measurements enable us to quantitatively determine the tissue averaged absorption and scattering coefficients and thus to impose constraints on the analysis of the CW data. The larger CW data sets (10^5 measurements) collected with a CCD permit 3D DOT reconstructions of a 1-liter tissue volume. Using a plane parallel transmission geometry the breast surface is imaged via a lens coupled CCD. This scheme reduces the complexity of the light channelling system to a single lens, instead of an array of fibers. For extrinsic contrast agents this is a natural imaging approach that has not been pursued to the clinical prototype by others.

Some form of optical tomography or image reconstruction must play a central role in any system which aims to use diffuse light to improve breast tumor diagnosis. Indeed the weakness in early (and current) clinical work is at least partially attributable to deficiencies in the image reconstruction approach. Various reconstruction approaches exist for DOT, (for a review see Arridge²⁶). In this work we employ a finite difference forward solver and use the explicit adjoint formulation for the inverse problem as described below. Most DOT approaches have been implemented in 2D. In the best 2D cases, researchers have employed a cylindrical geometry to reduce the dimensionality of the problem^{17-21,27}. Recently there have been direct comparisons between full 3D and 2D reconstructions using simulated data^{17,19,28}; not surprisingly the 3D reconstructions were superior. The main barrier for full

3D reconstruction is the significant memory and processing time it requires. For example, with 0.125mL voxels, 1L imaging domain, 10,000 measurements and a single pentium III processor our reconstructions take 24hrs. These numbers can vary by up to an order of magnitude depending on details of the algorithm. There are two steps of the algorithms that are costly: 1) solving the forward problem for each source position, detector position and/or frequency, 2) solving the inverse problem. We have chosen to solve these large-scale computational problems using parallel computing¹⁰ which reduces our reconstruction time from 24hrs to 2hrs.

The paper proceeds as follows. In the methods section we describe the experimental setup, the image reconstruction procedure, data analysis methods, tissue phantom experiments and *in vivo* measurement procedures. In the results and discussion section we evaluate and develop the relation between image noise and resolution for the system. We then proceed to evaluate object characterization, multiple object tomography, field of view, and spectral decomposition of multiple absorption images into constituent properties. *In vivo* results are discussed including measures of tissue averaged optical properties and differential imaging with a tumor target in the presence of physiologic fluctuations.

II. METHODS

A. Experimental

1. CCD transmission data:

In Fig. 1 we illustrate our clinical diffuse optical tomography table. For human measurements the subject lies on the table with both breasts suspended in a tank filled with the Intralipid. One breast is positioned central to the measurement area and held in soft compression between a movable compression plate and the viewing window. Four lasers operating at 690 nm, 750 nm, 786 nm, and 830 nm respectively are optically switched (Dicon Fiber Optics, GP700) between 45 fibers arranged on in a 9x5 square lattice within the

compression plate. The laser powers are balanced so typically $600 \pm 200 \mu W$ is delivered to the fiber tips for each of the four colors. The viewing window is modular and permits use of diffuse or anti-reflective coated transparent windows. A 50 mm $F\#=1.4$ lens (Nikkor AF 50mm F/1.4D) is used to image the detection plane onto the CCD chip with a magnification of 0.2. The light is detected by a thermoelectrically cooled ($-40^\circ C$) 1300x1340 CCD pixel array with area 2.6 cm x 2.68 cm (Roper Scientific, NTE1340). The CCD array is read with 16 bit A/D conversion. With a 800x1120 pixel ROI and 2x2 on chip binning the readout time is 300 ms. Concurrent frequency domain measurements are made with an array of 9 detectors fibers interlaced amongst the source fibers in the compression plate.

The signal-to-noise ratio (SNR) of the CCD light intensity measurements was evaluated using a Intralipid tissue phantoms with a range of different source detector plane distances (ΔY_{sd}). CCD measurements were binned into 24x24 square units to give an equivalent pixel size of 3.48 mm x 3.48 mm on the breast surface. A series of 100 measurements with 1 second exposure times were made on tissue phantoms with ($\mu_a = 0.05 cm^{-1}$ and $\mu'_s = 10 cm^{-1}$). The noise across the image plane was defined as the standard deviation for each binned pixel. For the source-detector plate separations of $\Delta Y_{sd} = 5$ to 7 cm, the SNR was greater than 10^3 for the peak signal pixel (i.e. pixel with shortest source-detector separation). For a pixel position located 6 cm from the peak signal pixel the SNR was 10^3 for $\Delta Y_{sd} = 6$ cm and 10^2 for $\Delta Y_{sd} = 7$. When the optical switch is switched between each frame the maximum SNR decreases to $2 * 10^2$. In our *in vivo* measurements of breast optical properties using a similar geometry most breast compressions were $6 \pm 1 cm^{29}$. Diffuse stray light contamination was present at a level of $\approx 10^{-4} * I_{peak}$. To avoid complications due to this light, data was cropped at $I/I_{peak} < 0.03$, keeping the stray light contribution $\leq 1\%$. For typical optical properties and source detector plate separations this intensity threshold cropped the data at a radius of 6 cm from the peak value. For the reconstructions the detector grid was defined as a 21x13 grid of measurements spaced 4.64 mm in both x and z directions spanning the region from $r_1 = \{-4.64 cm, y_d, -2.32 cm\}$ to $r_2 = \{4.64 cm, y_d, 2.32 cm\}$.

2. Frequency Domain

The light sources consist of the laser diodes described in the previous section (which are modulated at 70MHz). Light from the breast surface is channelled through 3 mm fiber bundles and measured by APD's (Hamamatsu C5330-4). The amplitude and phase of the detected diffuse photon density waves are obtained by demodulating the output of the APD using a homodyne technique³⁰. In our system the electrical signal from the APD passes through an amplifier (ZFL-500LN Mini-Circuits, gain=24dB), a band pass filter (BLP-70 Mini-Circuits), a computer controlled digital attenuator (ZFAT -51020 Mini-Circuits (0-36db)) and another amplifier (ZFL 500HLN, gain=19dB). An IQ demodulator (ZFMIQ-70D, 70 MHz, Mini-Circuits) followed by a low pass filter (SLP-1.9, Mini-Circuits) extracts phase and amplitude relative to the RF reference signal that drives the lasers. To minimize the cross-talk between various components, all of the electronics are placed in NIM boxes. The system is characterized by a noise equivalent power of $3pW/\sqrt{(Hz)}$, a linearity in amplitude of 1%, and phase drift of 0.25 degrees over 80 dB.

B. Theory

In this section we describe our forward model for light transport in tissue and our inverse solution scheme.

1. Forward model

We model light propagation through tissue and tissue phantoms with the diffusion approximation,

$$\nabla \cdot (D(\mathbf{r})\nabla\phi(\mathbf{r})) - (\mu_a(\mathbf{r}) - \frac{i\omega}{\nu})\phi(\mathbf{r}) = -S(\mathbf{r}). \quad (1)$$

Here $D(\mathbf{r}) = 1/3(\mu'_s(\mathbf{r}))$ is the diffusion coefficient, $\mu'_s(\mathbf{r})$ is the scattering coefficient. $\phi(\mathbf{r})$ is the photon fluence rate, $\mu_a(\mathbf{r})$ is the absorption coefficient, ν is the speed of light in the

media and ω is the source light modulation frequency. The source is characterized by an amplitude and phase { i.e. $S(r) = S_o e^{i\phi_o} \delta(r - r_s)$ }. Partial current boundary conditions are used on all surfaces:

$$\frac{\delta\phi(\mathbf{r})}{\delta\hat{n}} = -\alpha\phi(\mathbf{r}), \quad (2)$$

where $\alpha = \frac{(1-R_{eff})}{(1+R_{eff})} \frac{3\mu'_s}{2}$, where $R_{eff} \approx -1.440n^{-2} + 1.170n^{-1} + 0.668 + 0.063n$ and $n = \frac{n_{in}}{n_{out}}$.

The heterogenous diffusion equation is solved using a finite difference algorithm throughout a rectangular domain¹⁰. The rectangular volume is defined by $\mathbf{r}_{FV1} = \{-8, 0, -8\}$ and $\mathbf{r}_{FV2} = \{8, 6, 8\}$ with elements $\{Nx, Ny, Nz\} = \{65, 25, 65\}$ of size $\{\Delta x, \Delta y, \Delta z\} = \{0.25, 0.25, 0.25\}$ cm for a total of 105,625 grid points.

2. Image reconstructions

We describe our reconstruction scheme for absorbing heterogeneities only. Our approach is based on the diffusion equation (Eq. 1) and involves minimizing a Rytov type least squared error between calculated and measured photon densities for each source detector pair³¹⁻³³. Optode pair measurements (indexed by i) are indicated by the source and detector positions $(\mathbf{r}_{di}, \mathbf{r}_{si})$. The error function minimized is (see Engl et al.³⁴),

$$\min\{||\ln\{\frac{\phi_m}{\phi_{mR}}\} - \ln\{\frac{\phi_c}{\phi_{cR}}\}||_2^2 + Regularization\}. \quad (3)$$

The measured photon fluence rates for a reference medium and the medium of interest are $\phi_{mR}(\mathbf{r}_{di}, \mathbf{r}_{si})$ and $\phi_m(\mathbf{r}_{di}, \mathbf{r}_{si})$ respectively. Similarly $\phi_{cR}(\mathbf{r}_{di}, \mathbf{r}_{si})$ and $\phi_c(\mathbf{r}_{di}, \mathbf{r}_{si})$ are the respective "reference" and "of interest" calculated fields. The regularization term is discussed below. $\phi_{cR}(\mathbf{r}_{di}, \mathbf{r}_{si})$ is calculated using apriori information, (usually the Intralipid mixture optical properties and tank geometry). $\phi_c(\mathbf{r}_{di}, \mathbf{r}_{si})$ however is computed based on the unknown properties that we wish to determine; it's calculation requires inversion the techniques.

To determine $\phi_c(\mathbf{r}_{di}, \mathbf{r}_{si})$ we used an iterative method, with linear Rytov update steps. We defined $\phi_c^{k+1}(\mathbf{r}_{di}, \mathbf{r}_{si}) = \phi_c^k(\mathbf{r}_{di}, \mathbf{r}_{si}) \exp(\phi_{scat}^{k+1}(\mathbf{r}_{di}, \mathbf{r}_{si}))$, where k is the iteration index and

$\phi_c^o(\mathbf{r}_{di}, \mathbf{r}_{si})$ is calculated using an initial guess of the optical properties. The Rytov scattered wave for a particular source detector pair, $\phi_{scat}^{k+1}(\mathbf{r}_{si}, \mathbf{r}_{di})$ is thus,

$$-\ln\left(\frac{\phi_c^{k+1}(\mathbf{r}_{di}, \mathbf{r}_{si})}{\phi_c^k(\mathbf{r}_{di}, \mathbf{r}_{si})}\right) = \frac{\nu}{D} \frac{\int G_c^k(\mathbf{r}_{di}, \mathbf{r}) G_c^k(\mathbf{r}, \mathbf{r}_{si}) \Delta\mu_a^{k+1}(\mathbf{r}) d^3r}{G_c^k(\mathbf{r}_{di}, \mathbf{r}_{si})}. \quad (4)$$

Here $\phi_c^k(\mathbf{r}, \mathbf{r}_{si})$ is the solution to the diffusion equation for a light source at position \mathbf{r}_{si} and a specified distribution of absorption $\mu_a^k(\mathbf{r})$ and scattering $\mu_s'(\mathbf{r})$. The Greens function $G_c^k(\mathbf{r}_{di}, \mathbf{r})$ is the solution to the diffusion equation for a delta function source at the location of the i^{th} detector, ($S = \delta(\mathbf{r}_{di} - \mathbf{r})$), and the same distributions of absorption, $\mu_a^k(\mathbf{r})$, and scattering, $\mu_s'(\mathbf{r})$. The differential absorption ($\Delta\mu_a^{k+1}(\mathbf{r})$) is the unknown vector we seek.

Equation 4 can be transformed into the following matrix equation,

$$-\ln\left\{\frac{\phi_c^{k+1}}{\phi_c^k}\right\} = [\mathbf{J}^k] \{\Delta\mu_a^{k+1}\}^T. \quad (5)$$

The Jacobian ($[\mathbf{J}^k] = \left[\frac{\delta \ln\{\phi_c^k\}}{\delta \mu_a}\right]$) is explicitly generated using an adjoint method.

$$\left(\frac{\delta \ln\{\phi_c^k\}}{\delta \mu_a}\right)_{ij} = \frac{\nu}{D} \frac{G_c^k(\mathbf{r}_{di}, \mathbf{r}_j) G_c^k(\mathbf{r}_j, \mathbf{r}_{si})}{G_c^k(\mathbf{r}_{di}, \mathbf{r}_{si})} \quad (6)$$

where \mathbf{r}_j is the voxel position.

We follow a Morse-Penrose pseudoinverse approach in which a square matrix is created by multiplying both sides of the forward problem by the transpose of the Jacobian. The inversion is stabilized using a spatially variant Tikhonov regularization scheme. With substitution of ϕ_c^{k+1} for ϕ_c the objective function (Eq. 3) used for each iteration inverse step becomes;

$$\min\left\{\left\|\ln\left\{\frac{\phi_m}{\phi_{mR}}\right\} - \ln\left\{\frac{\phi_c^k}{\phi_{cR}}\right\} + [\mathbf{J}^k] \{\Delta\mu_a^{k+1}\}^T\right\|_2^2 + \lambda(\mathbf{r}) \|\{\Delta\mu_a^{k+1}\}\|_2^2\right\}. \quad (7)$$

This can be arranged in a more compact form;

$$\min\left\{\left\|[\mathbf{J}^k] \{\Delta\mu_a^{k+1}\}^T + \ln\left\{\frac{\phi_m}{\phi_{mR}} \frac{\phi_{cR}}{\phi_c^k}\right\}\right\|_2^2 + \lambda(\mathbf{r}) \|\{\Delta\mu_a^{k+1}\}\|_2^2\right\}. \quad (8)$$

The related matrix equation to be inverted for each iteration step is

$$([\mathbf{J}^k]^T [\mathbf{J}^k] + \lambda(\mathbf{r}) [\mathbf{I}]) \{\Delta\mu_a^{k+1}\}^T = -[\mathbf{J}^k]^T \ln\left\{\frac{\phi_m}{\phi_{mR}} \frac{\phi_{cR}}{\phi_c^k}\right\}. \quad (9)$$

This matrix equation is solved using a conjugate gradient method. The result of one inverse solve is an updated set of optical properties. The optical property map from the preceding iteration is used as the basis for a finite difference forward solve and construction of the Jacobian for each iteration. The regularization constants defined below were held constant at each step. Convergence was found to be consistently obtained after fifteen iterations.

Following Pogue et al³⁵ we use spatially variant regularization. We implement the method in the plane parallel geometry using a spatially variant regularization parameter controlled by center (l_c) and edge (l_e) parameters according to the following formula.

$$\lambda(\mathbf{r}) = l_c + l_e * (e^{-\rho_x/R_x} + e^{-\rho_y/R_y} + e^{-\rho_z/R_z} - 3) \quad (10)$$

Here, $\rho_x = \|r_x\|$, $\rho_y = \|r_y - 3\|$, $\rho_z = \|r_z\|$, and $R_x = 16$, $R_y = 6$, $R_z = 16$. A ratio of $l_e/l_c = 10$ was empirically determined to produce even image noise as a function of depth from the source and detector planes. Finally, the inversion volume was performed over a mesh volume defined by $\mathbf{r}_{IV1} = \{-6, 0, -6\}$ and $\mathbf{r}_{IV2} = \{6, \delta Y_{sd}, 6\}$ with elements $\{nx, ny, nz\} = \{24, 12, 24\}$ of size $\{\delta_x, \delta_y, \delta_z\} = \{0.5, 0.5, 0.5\}$ cm.

C. Phantom measurements

Tissue phantom imaging experiments were used to evaluate the imaging performance of our machine. All phantom tests were performed using a background Intralipid/ink tissue phantom with a $\mu_a(\lambda(786 \text{ nm})) = 0.05 \text{ cm}^{-1}$ and $\mu'_s(\lambda(786 \text{ nm})) = 8 \text{ cm}^{-1}$. Silicone rubber tissue phantoms were used to create solid shapes for two purposes. To avoid problems related to the phenomena of a tissue air interface near our imaging domain, we extended the diffuse media vertically by placing a solid tissue phantom above the compression plate area. When a subject is in the machine, the chest wall plays a similar role. The tissue phantom top used in these measurements had $\mu_a(\lambda(786 \text{ nm})) = 0.067 \text{ cm}^{-1}$ and $\mu'_s(\lambda(786 \text{ nm})) = 13 \text{ cm}^{-1}$. The solid tissue phantoms were also used as imaging targets. The targets were cut from 500 ml homogeneous solid blocks with prescribed optical properties and suspended in Intralipid with thin white thread at prescribed positions.

A final group of indocyanine green (ICG) phantom measurements employed a pair of flow cells. They were cylinders with inside diameter 1.6 cm, inside length 1.6 cm, and wall thickness of 0.5 mm. In general the objects were placed in pairs as depicted in Fig. 2, with positions $\mathbf{r}_{obj1} = \{-2.5, 3, 0\}$ and $\mathbf{r}_{obj2} = \{2.5, 3, 0\}$.

D. *In vivo* measurements

In vivo measurements evaluated system performance for obtaining background optical properties of breast tissue, differential imaging in the presence of physiologic fluctuations. All measurements with humans were performed in accordance with Univ. of Pennsylvania IRB protocol, # 700394. The tissue averaged optical properties of breast were obtained from a central subset of the frequency domain measurements that predominantly sampled the breast tissue. One healthy subject age 25 was measured. The compressed breast shape was a half ellipsoid measuring 13 cm at the top of the compression plate and extending 10 cm below the top source. The subset consisted of central sources near the four detectors that were more than 2 cm away from the breast/Intralipid boundary. The data was analyzed by approximating the breast geometry as a homogenous slab. The measurement was repeated 10 times.

To simulate a contrast agent injection, we made differential measurements with and without a target (diameter= 1cm, $\mu_a = 0.2 \text{ cm}^{-1}$) taped externally on the side of the breast. Background measurements were taken after removing the target. This simulates the ideal contrast agent injection. The scattered wave was constructed using $\phi_m = \phi_{target-on}$ and $\phi_{m0} = \phi_{target-off}$. The measured breast tissue averaged optical properties were assumed for the entire volume. Although this assumption generates a model mismatch in the Intralipid volume, such assumptions have been shown to be useful simplifications in differential imaging applications^{2,16}.

III. RESULTS

A. Point Spread Functions

We evaluated resolution performance of our system using point spread function (PSF) measurements. In these tests we measured the reconstruction size (FWHM) of point-like objects. For any measurement, the extent of the PSF can be reduced. The cost of better resolution however is increased image noise. Our experiments thus also evaluate the resolution-vs-image noise relation. We used small strongly absorbing point like objects, specifically 4 mm diameter spheres with $\mu_a = 2.0 \text{ cm}^{-1}$ and $\mu'_s = 8 \text{ cm}^{-1}$. These objects have a linear signal strength ($\delta\mu_a * \text{volume} = 0.07 \text{ cm}^2$) which is similar to the linear signal strength of an object with 1 cc volume and a $\delta\mu_a = 0.07 \text{ cm}^{-1}$. Two such objects were arranged at $\mathbf{r}_1 = \{-2.5, 3, 0\}$, and $\mathbf{r}_2 = \{2.5, 3, 0\}$

Reconstructions were performed for a range of regularization constants, $l_c = \{1000, 100, 10, 1, 0.1, 0.01, 0.001\}$. Figure 3 depicts a reconstruction with $l_c = 0.1$. Plots of object cross-sections and a histogram of the image intensity values for a range of regularization constants (Fig. 4) illustrate the effects of regularization. The cross-sections are evaluated at the FWHM. The dispersion of the image intensities indicate image noise. Generally the histogram is the sum of a symmetrically dispersed distribution of image noise and a secondary distribution at high μ_a due to the objects. This can be seen by considering the isosurface (see Fig. 3a) drawn at 1/2 maximum contrast.

There is generally a trade off between resolution and image noise. This is summarized in Fig. 5a. where we plot FWHM -vs-image noise. The regularization constant parameterizes the curve. At a preliminary level of analysis the entire curve defines system performance. A viewer may choose to interpret the data at any point on the curve, trading resolution for image noise. However it is preferable to establish the optimal image. There are several parameter choice methods for establishing the optimal regularization parameter. We considered three approaches.

An empirical approach is to define an image noise level that can be tolerated for a particular imaging question³³. For instance, $\langle \delta\mu_a \rangle \leq 0.0025$, would set the regularization constant at $l_c = 0.1$ and correspondingly the FWHM at 1.2 cm.

A parameter choice approach called L-curve analysis provides a method of effectively calculating the regularization constant directly from the measurements³⁴. L-curve analysis examines the parametric relation between the image norm, the measurement error norm, and the regularization constant. In equation 8 the regularization parameter, $\lambda(\mathbf{r})$, controls the relative weight between the image variance norm and the measurement error norm. L-curve analysis plots these two norms against each other for the range of regularization parameters (see Fig. 5b). The result is an L shaped curve with the knee of the curve representing an optimal regularization value. This analysis places the regularization at $l_c = 1.0$.

Third we considered an approach in which the ratio between the object contrast and the image noise (CNR) is maximized. We plot CNR vs regularization constant in Fig. 5c. The CNR peaks at $l_c = 0.1$. This corresponds to one decade lower than the L-curve analysis. Since the contrast-to-noise value is a more tangible optimization, we proceed with $l_c = 0.1$ as the optimal regularization constant. It appears that L-curve analysis provides an overly-smooth solution for the imaging situation of two isolated point objects in a relatively large imaging domain. When $l_c = 0.1$ we obtain a 3D point spread function with $FWHM = \{1.1, 1.13, 1.1\}$ combined with an image noise of $\langle \delta\mu_a \rangle = 0.0024 \text{ cm}^{-1}$. Since the objects are 4 mm in diameter the peak contrast value is considerably lower than the physical target object contrast ($\frac{\langle \delta\mu_a \rangle_{recon}}{\langle \delta\mu_a \rangle_{object}} = \frac{0.098}{2} = 0.049$). However the integrated signal, $Sig = \mu_a * volume$ is closer to expectation with ($\frac{Sig_{recon}}{Sig_{object}} = \frac{0.0265}{0.0650} = 0.41$). Since the signal strength does not vary linearly with μ_a for large μ_a , this discrepancy in integrated signal strength is reasonable.

B. Characterization

Diffuse optical tomography is an inherently non-linear imaging method. Although point spread functions are useful, one cannot be certain that a new object will show up as the original convolved with the PSF. It is therefore best to check questions of interest directly. In breast cancer studies one aims to use DOT to characterize a suspicious mass. Our goal here is to evaluate whether the volume integrated signal is quantitative for objects smaller than the optimized PSF of the machine. This series of measurements evaluates characterization of spherical objects with small differential contrast $\frac{\delta\mu_a}{\mu_a} = 3$. In particular we reconstruct objects of three different sizes; 5 mm, 10 mm and 15 mm spheres, with $\mu_a = 0.2$. The results are shown in Fig. 6. The image of the 15 mm sphere shows an object close to the correct size and with moderately lower μ_a value, ($\frac{\langle\delta\mu_a\rangle_{recon}}{\langle\delta\mu_a\rangle_{object}} = 0.73$, $\frac{Sig_{recon}}{Sig_{object}} = \frac{0.31}{0.27} = 1.16$). Images of both the 5mm target ($\frac{\langle\delta\mu_a\rangle_{recon}}{\langle\delta\mu_a\rangle_{object}} = 0.09$, $\frac{Sig_{recon}}{Sig_{object}} = \frac{0.011}{0.009} = 1.16$) and 10mm target ($\frac{\langle\delta\mu_a\rangle_{recon}}{\langle\delta\mu_a\rangle_{object}} = 0.23$, $\frac{Sig_{recon}}{Sig_{object}} = \frac{0.083}{0.078} = 1.06$) depict objects larger and with significantly lower μ_a than the targets, reflecting a smoothing operation consistent with the optimized PSF. However, the volume integrated signal of the objects show much better agreement with the expected values.

C. Field of View

In this section we evaluate the ability of the system to image an extended tissue volume and to reconstruct a heterogeneous medium with multiple objects. We dispersed 15 cubic silicone tissue phantom objects throughout the measurement volume. The 8 mm edge dimension cubes with $\mu_a = 0.2 \text{ cm}^{-1}$, $\mu'_s = 10 \text{ cm}^{-1}$ were arranged in a hexagonal lattice. Single wavelength ($\lambda = 786 \text{ nm}$) measurements were taken with and without the objects present and reconstructions were performed with $l_c = 0.1$. The resulting 3D reconstructed volume is depicted in Fig. 7 with isosurfaces at $\mu_a = 0.092 \text{ cm}^{-1}$. The results are also shown in cross-sections at y depths of 1.5 cm, 3cm and 4.5 cm. Note that the objects are

well separated in all three dimensions and that only objects that belong in each plane are present. There is a small amount of ghosting between the slices, but this is consistent with the z-direction FWHM found in the point spread function. The peak values drop to 75% of the center values for objects on the edges of the reconstruction volume. The resolution is optimal at the central xz values and improves towards the source and detector plane. However the spatially variant regularization has provided fairly consistent sensitivity and resolution throughout a volume with dimensions {16,6,5} cm.

D. Spectroscopy

The next set of measurements evaluate the ability to characterize the constituent concentrations of a tissue phantom. Two 3.2 cc flow cells were used, one with an ink contrast and the other with an ICG contrast. Reconstructions were performed at all four wavelengths. The absorption maps were then combined into concentration maps on a voxel by voxel basis using $\vec{C}(\mathbf{r}_v) = E^{-1}\vec{\delta\mu}_a(\mathbf{r}_v)$. Here $\vec{\delta\mu}_a(\mathbf{r}_v) = \{\delta\mu_a(\mathbf{r}_v)^{\lambda 690}, \delta\mu_a(\mathbf{r}_v)^{\lambda 750}, \delta\mu_a(\mathbf{r}_v)^{\lambda 786}, \delta\mu_a(\mathbf{r}_v)^{\lambda 830}\}$, is a vector containing the $\delta\mu_a$ values at \mathbf{r}_v for each wavelength, E is a matrix containing the extinction coefficients of ink, and indocyanine green at the four wavelengths, and $\vec{C}(\mathbf{r}_v) = \{[ICG](\mathbf{r}_v), [Ink](\mathbf{r}_v)\}$ is a vector containing the concentrations at each voxel. The $\delta\mu_a$ and concentration images are shown in Fig. 9. Note that both objects appear in all four of the absorption images. However the concentration images successfully distinguish between the india ink and the indocyanine green dye. These results, combined with the object characterization results, suggest that even for tumors smaller than the resolution of our machine (diameter 5mm), this DOT system will correctly determine the tissue chromophore concentrations when averaged over the volume of the PSF (e.g. the volume integrated values are correct). We anticipate similar spectral decomposition performance in obtaining ICG concentrations and hemoglobin concentrations in clinical imaging situations.

E. *In vivo* average breast properties

Transillumination images of a breast are shown in Fig. 10. The breast position and outline are obtained from these images. The average breast tissue properties are derived from the FD data at four wavelengths. The data was analyzed with a semi-infinite diffusion model. The data and semi-infinite fits for a 25 year old subject are shown in Fig. 11. We find good agreement with the semi-infinite model for the range of source-detector separations chosen. The absorption and scattering coefficients obtained are plotted in Fig. 12. The error bars represent the standard deviation of the absorption and scattering coefficients from ten measurements. The hemoglobin concentrations can be obtained through spectral decomposition assuming a 50/50 lipid/water concentration where the lipid spectra is from reference³⁶ and the water spectra is from reference³⁷. These hemoglobin concentrations are consistent with values we have obtained using a scanning transmission RF machine²⁹. Our numbers are also in reasonable agreement with the results of other groups using a variety of measurement types and geometries^{3,5,38}

The differential image experiments were reconstructed and yield the images shown in Fig. 13. The system is clearly capable of imaging tumor like targets in the presence of physiologic fluctuations. The image has more structure than the Intralipid phantom images of equivalent targets (Fig. 3). This structure is most probably a result of physiologic fluctuations that propagate into the image as noise. We compare the dispersion of the voxel values for phantom and *in vivo* imaging in Fig. 14. The image variance in the *in vivo* measurements is 4.3 times larger than for Intralipid. This illustrates two points about the machine. First, the measurements obtained with the lens coupled CCD have sufficient SNR (i.e. measurement noise is not the leading cause of image noise for an *in vivo* measurement). Secondly, even in the presence of physiologic fluctuations on the time scale of minutes, we can produce images with contrast-to-noise ratios sufficient to image tumors in human breast.

IV. DISCUSSION

Diffuse optical tomography utilizes inherently 3D measurements of tissue volumes. In order for the technique to progress towards clinical utility it is important to develop instruments that provide full 3D imaging of the entire breast tissue volume. Furthermore, in such cases it becomes challenging to acquire and process a sufficiently large data set. In this paper we evaluated a novel hybrid CCD based DOT system with parallel computation for image reconstruction. This scheme provides imaging of Liter tissue volumes with 5 mm voxel size and 1 cm resolution. Generally, when DOT systems use CCD detection, CCD elements are coupled to tissue surfaces using discrete fibers. We have demonstrated DOT performance using single lens coupling. This scheme has several advantages. Uncertainty in the calibration of the detectors coupling can often degrade image quality³⁹. These coupling coefficients can be obtained at the cost of increasing the number of unknowns in the image reconstruction process. By using a single detection element and contact surface (imaging window) the number of calibration coefficients are significantly reduced (ideally to one detector coefficient). This is evident in the fact that the dominating systematic noise source in our device is the source fiber switching mechanism. The high resolution of the underlying CCD measurement also facilitates two standard and relevant CCD features. The pixel binning is flexible allowing for effortless exchange of detector area for sampling density, and the high resolution imaging permits an standard reflectance image of the breast from which the breast shape and particular boundary positions can be obtained. This knowledge can potentially be translated into *a priori* information for image reconstruction.

A second theme of this paper has been the characterization of our DOT device. To this end we employed an evaluation procedure that should have general relevance to DOT systems. Using tissue phantoms, we have evaluated the system for point spread function resolution, object characterization, multiple object tomography, field of view and spectral decomposition. A critical component of the evaluation procedure was the optimization of the relation between image noise and resolution for system parameters relevant to breast tumor

imaging. Though the underlying physical models for DOT are nonlinear, we found that PSF derived generally describes the performance of the machine. This illustrates the manner in which DOT is ill-posed when constrained to absorption only perturbations. For absorption imaging, the ill-posed nature of DOT consists of a blurring process that can be conceptually and quantitatively captured in a simple localized point spread function characterization for most breast imaging situations. Related analytic studies by Schotland et al. explore similar point spread function use²⁵.

For comparison with other groups we consider the ratio of the apparent object size (related to the FWHM of a PSF) divided by the depth of the object. We use this as an approximate measure of imaging performance with smaller ratios indicating better resolution. The system described in this paper obtains an object to depth ratio of 1/2.8. Jiang et al., have reconstructed three dimensional images of tissue phantoms and tumors in breast^{4,19}. Using a 16 source, 16 detector continuous wave instrument, 10 mm phantom objects were accurately reconstructed at a depth of 1.3 cm from the measurement surface giving an object to depth ratio of $<1/1.4$. The ratio may underestimate the resolution performance of their machine (i.e. they didn't look at smaller objects). In addition, they have obtained similar performance with *in vivo* images of tumors⁴. Pogue et al. have reported a considerable amount of work in 2D and recently explored the effects of 3D^{3,28,40,41}. Using a 16 source, 16 detector frequency domain system 4 mm rods were correctly characterized at a depth of 2 cm (with object contrast of 4:1). The resulting ratio of object to depth, 1/5, is very good. Note, these results are for cylinders which have higher integrated contrasts than spheres. When they look at spherical objects, the object contrast drops for sizes below 1.5 cm²⁸. Hawrysz et al have reconstructed three dimensional fluorescent objects with an error handling scheme using a 4 source, 46 detector system⁴². With this system, 1 cm objects were reconstructed at a depth of 2 cm giving an object to depth ratio of $< 1/2$. Hebden et al have used a 32 source, 32 detector time resolved system to reconstruct fairly low contrast objects and separate both absorption and scattering contrasts in a conical breast imaging geometry¹⁷. This is a particularly difficult imaging task. Here they find 1 cm objects reconstruct to twice

the actual size (8 times larger volume) at a depth of 2.1cm, resulting in an object to depth ratio of 1. Ueda et al, also use a 32 source 32 detector time resolved system to image 1 cc objects⁴³. With objects at depths 10 mm, 30 mm and 15 mm the system obtains FWHM values of 13.8, 20.26, and 23.5mm. The resulting object/depth ratios were, 1/0.72, 1/1.48, and 1/ 0.74 respectively. The different contrasts, data types, and prior constraints concerning the absorption and scattering of objects, complicate comparisons across these different groups. We note though, that time-resolved systems, perhaps due to system complexity, generally produce higher object/depth ratios than the CW and frequency-domain systems. Since time-resolved systems inherently have more complete information, we anticipate time-resolved performance to improve as systems become better optimized.

Finally *in vivo* studies of healthy subjects with our system evaluated repeatability of average tissue optical properties and differential imaging performance. One of the drawbacks of obtaining large measurement sets is the lower sampling rate. Our current measurements take 4 minutes per color. Significantly the physiologic fluctuations, while degrading the image quality by a measurable amount, did not corrupt the general localizing capabilities. In addition these results suggest that the measurement noise has been sufficiently reduced and is not a limiting factor in the image reconstruction process for differential measurements. Based on these comprehensive evaluation studies we anticipate this system and systems of similar design will provide clinically useful quantitative 3D images of breast.

V. ACKNOWLEDGEMENTS

We gratefully acknowledge support from grants NIH RO1-CA75124-04, and Army BC9907335.

VI. REFERENCES

REFERENCES

- ¹ D. A. Benaron, S. R. Hintz, A. Villringer, D. Boas, A. Kleinschmidt, J. Frahm, C. Hirth, H. Obrig, J. C. van Houten, E. L. Kermit, W. F. Cheong, and D. K. Stevenson, "Noninvasive functional imaging of human brain using light", *J. Cereb. Blood Flow Metab.* **20**, 469 (2000).
- ² S. B. Colak, M. B. van der Mark, G. W. Hooft, J. H. Hoogenraad, E. S. van der Linden, and F. A. Kuijpers, "Clinical optical tomography and NIR spectroscopy for breast cancer detection", *IEEE J. Sel. Top. Quantum Electron.* **5**, 1143 (1999).
- ³ B. W. Pogue, S. P. Poplack, T. O. McBride, W. A. Wells, K. S. Osterman, U. L. Osterberg, and K. D. Paulsen, "Quantitative hemoglobin tomography with diffuse near-infrared spectroscopy: pilot results in the breast", *Radiology*, **218**, 261 (2001)
- ⁴ H. Jiang, Y. Xu, N. Iftimia, J. Eggert, K. Klove, L. Baron, and L. Fajardo, "Three-dimensional optical tomographic Imaging of breast in a human subject", *IEEE Trans. Med. Imaging* **20**, 1334 (2001).
- ⁵ V. Ntziachristos, A. G. Yodh, M. Schnall, and B. Chance, "Concurrent MRI and diffuse optical tomography of breast after indocyanine green enhancement", *Proc. Natl. Acad. Sci. U. S. A.* **97**, 2767 (2000).
- ⁶ H. Wallberg, "Diaphanography in various breast disorders. Clinical and experimental observations", *Acta Rad. Diag.* **26**, 129 (1985).
- ⁷ A. E. Profio, "Scientific basis of breast diaphanography", *Med. Phys.* **16**, 60 (1989).
- ⁸ X. H. Zhou, "Detection of early breast cancer: an overview and future prospects", *Crit. Rev. Bio. Eng.* **17**, 203 (1989).
- ⁹ M. A. Franceschini, K. T. Moesta, S. Fantini, G. Gaida, E. Gratton, H. Jess, W. W. Mantulin, M. Seeber, P. M. Schlag, and M. Kaschke, "Frequency-domain techniques enhance

- optical mammography: Initial clinical results", *Proc. Natl. Acad. Sci. U. S. A.* **94**, 6468 (1997).
- ¹⁰ M. J. Holboke, B. J. Tromberg, X. Li, N. Shah, J. Fishkin, D. Kidney, J. Butler, B. Chance, and A. G. Yodh, "Three-dimensional diffuse optical mammography with ultrasound localization in a human subject", *J. Biomed. Opt.* **5**, 237 (2000).
 - ¹¹ M. Gurfinkel, A. B. Thompson, W. Ralston, T. L. Troy, A. L. Moore, T. A. Moore, J. D. Gust, D. Tatman, J. S. Reynolds, B. Muggenburg, K. Nikula, R. Pandey, R. H. Mayer, D. J. Hawrysz, and E. M. Sevick-Muraca, "Pharmacokinetics of ICG and HPPH-car for the detection of normal and tumor tissue using fluorescence, near-infrared reflectance imaging: A case study", *Photochem. Photobiol.* **72**, 94 (2000).
 - ¹² R. Weissleder and U. Mahmood, "Molecular Imaging [Review]", **219(2)**, 316 (2001).
 - ¹³ J. P. Culver, V. Ntziachristos, M. J. Holboke, and A. G. Yodh, "Optimization of optode arrangements for diffuse optical tomography: A singular-value analysis", *Opt. Lett.* **26**, 701 (2001).
 - ¹⁴ M. Patterson, B. Chance, and B. Wilson, "Time resolve reflectance and transmittance for the noninvasive measurement of tissue optical properties.", *Appl. Opt.*, **28**, 2331 (1989).
 - ¹⁵ S. R. Arridge and W. R. B. Lionheart, "Nonuniqueness in diffusion-based optical tomography", *Opt. Lett.* **23**, 882 (1998).
 - ¹⁶ V. Ntziachristos, B. Chance, and A. G. Yodh, "Differential diffuse optical tomography", *Opt. Express* **5**, 230 (1999).
 - ¹⁷ J. C. Hebden, H. Veenstra, H. Dehghani, E. M. C. Hillman, M. Schweiger, S. R. Arridge, and D. T. Delpy, "Three-dimensional time-resolved optical tomography of a conical breast phantom", *Appl. Optics* **40**, 3278 (2001).
 - ¹⁸ E. M. Hillman, J. C. Hebden, M. Schweiger, H. Dehghani, F. E. Schmidt, D. T. Delpy,

- and S. R. Arridge, "Time resolved optical tomography of the human forearm", *Phys Med Biol* **46**, 1117 (2001).
- ¹⁹ H. B. Jiang, Y. Xu, and N. Iftimia, "Experimental three-dimensional optical image reconstruction of heterogeneous turbid media from continuous-wave data", *Opt. Express* **7**, 204 (2000).
- ²⁰ C. H. Schmitz, H. L. Graber, H. B. Luo, I. Arif, J. Hira, Y. L. Pei, A. Bluestone, S. Zhong, R. Andronica, I. Soller, N. Ramirez, S. L. S. Barbour, and R. L. Barbour, "Instrumentation and calibration protocol for imaging dynamic features in dense-scattering media by optical tomography", *Appl. Optics* **39**, 6466 (2000).
- ²¹ T. O. McBride, B. W. Pogue, S. Jiang, U. L. Osterberg, and K. D. Paulsen, "A parallel-detection frequency-domain near-infrared tomography system for hemoglobin imaging of the breast in vivo", *Rev. Sci. Instrum.* **72**, 1817 (2001).
- ²² K. T. Moesta, S. Totkas, S. Fantini, H. Jess, M. Kaschke, and P. M. Schlag, "Frequency domain laser scanning mammography of the breast - First clinical evaluation study", *Eur. J. Cancer* **33**, 358 (1997).
- ²³ X. D. Li, D. N. Pattanayak, T. Durduran, J. P. Culver, B. Chance, and A. G. Yodh, "Near-field diffraction tomography with diffuse photon density waves", *Phys. Rev. E* **61**, 4295 (2000).
- ²⁴ V. A. Markel and J. C. Schotland, "Inverse problem in optical diffusion tomography. I. Fourier- Laplace inversion formulas", *J. Opt. Soc. Am. A-Opt. Image Sci. Vis.* **18**, 1336 (2001).
- ²⁵ J. C. Schotland and V. A. Markel, "Inverse scattering with diffusing waves", *J. Opt. Soc. Am. A-Opt. Image Sci. Vis.* **18**, 2767 (2001).
- ²⁶ S. R. Arridge, "Optical tomography in medical imaging", *Inverse Probl.* **15**, R41 (1999).

- ²⁷ B. W. Pogue, M. S. Patterson, H. Jiang, and K. D. Paulsen, "Initial Assessment of a Simple System For Frequency-Domain Diffuse Optical Tomography", *Phys. Med. Biol.* **40**, 1709 (1995).
- ²⁸ B. W. Pogue, S. Geimer, T. O. McBride, S. D. Jiang, U. L. Osterberg, and K. D. Paulsen, "Three-dimensional simulation of near-infrared diffusion in tissue: boundary condition and geometry analysis for finite- element image reconstruction", *Appl. Optics* **40**, 588 (2001).
- ²⁹ T. Durduran, R. Choe, J. P. Culver, L. Zubkov, B. Chance, and A. Yodh, "Bulk optical properties of healthy female tissue," ,submitted for publication.
- ³⁰ Y. S. Yang, H. L. Liu, X. D. Li, and B. Chance, "Low-cost frequency-domain photon migration instrument for tissue spectroscopy, oximetry, and imaging", *Opt. Eng.* **36**, 1562 (1997).
- ³¹ C. P. Gonatas, M. Ishii, J. S. Leigh, and J. C. Schotland, "Optical Diffusion Imaging Using a Direct Inversion Method", *Phys. Rev. E* **52**, 4361 (1995).
- ³² J. C. Hebden, D. J. Hall, M. Firbank, and D. T. Delpy, "Time-Resolved Optical Imaging of a Solid Tissue-Equivalent Phantom", *Appl. Optics* **34**, 8038 (1995).
- ³³ M. A. O'Leary, D. A. Boas, B. Chance, and A. G. Yodh, "Experimental Images of Heterogeneous Turbid Media By Frequency- Domain Diffusing-Photon Tomography", *Opt. Lett.* **20**, 426 (1995).
- ³⁴ H. W. Engl, M. Hanke, and A. Neubauer, *Regularization of Inverse Problems* (Kluwer Academic, Dordrecht, 1996).
- ³⁵ B. W. Pogue, T. O. McBride, J. Prewitt, U. L. Osterberg, and K. D. Paulsen, "Spatially variant regularization improves diffuse optical tomography", *Appl. Optics* **38**, 2950 (1999).
- ³⁶ R. Cubeddu, "Effects of the menstrual cycle on the red and near-infrared optical properties

- of the human breast", *Photochem. Photobio.* **72**, 383 (2000).
- ³⁷ G. Hale and M. Querry, "Optical Constants of Water in the 200 nm 200 um region", *Appl. Optics* **12**, 555 (1973).
- ³⁸ N. Shah, A. Cerussi, C. Eker, J. Espinoza, J. Butler, J. Fishkin, R. Hornung, and B. Tromberg, "Noninvasive functional optical spectroscopy of human breast tissue", *Proc. Natl. Acad. Sci.* **98**, 4420 (2001).
- ³⁹ D. A. Boas, T. Gaudette, and S. R. Arridge, "Simultaneous imaging and optode calibration with diffuse optical tomography", *Opt. Express* **8**, 263 (2001).
- ⁴⁰ T. O. McBride, B. W. Pogue, S. D. Jiang, U. L. Osterberg, K. D. Paulsen, and S. P. Poplack, "Initial studies of in vivo absorbing and scattering heterogeneity in near-infrared tomographic breast imaging", *Opt. Lett.* **26**, 822 (2001).
- ⁴¹ B. W. Pogue, C. Willscher, T. O. McBride, U. L. Osterberg, and K. D. Paulsen, "Contrast-detail analysis for detection and characterization with near-infrared diffuse tomography", *Med. Phys.* **27**, 2693 (2000).
- ⁴² D. J. Hawrysz, M. J. Eppstein, J. W. Lee, and E. M. Sevick-Muraca, "Error consideration in contrast-enhanced three-dimensional optical tomography", *Opt. Lett.* **26**, 704 (2001).
- ⁴³ Y. Ueda, K. Ohta, M. Oda, M. Miwa, Y. Tsuchiya, and Y. Yamashita, "Three-dimensional imaging of a tissuelike phantom by diffusion optical tomography", *Appl. Optics* **40**, 6349 (2001).

FIGURES

FIG. 1. a) Schematic of clinical DOT table. b&c) Pictures of the instrument. The subject lies on the table with both breasts suspended in the Intralipid tank and positions one breast central to the measurement area. The breast is held in soft compression between a movable compression plate and viewing window. Laser light sources are optically switched between 45 fibers arranged on in a 9x5 square lattice within the compression plate. The modular viewing window can be fitted with either diffuse or anti-reflective coated transparent windows. The transmitted light is detected by a TE cooled, 2.6 cm x 2.68 cm, lens coupled CCD. Simultaneous frequency domain measurements are made with an array of 9 detectors fibers interlaced amongst the source fibers in the compression plate.

FIG. 2. Schematic of reconstruction volume. Sources are located in the $y=0$ plane the detectors are located on the $y=6$ cm plane. The position of two typical target phantoms is indicated. a) An isosurface rendering combined with slices through three orthogonal planes. The slices are individually rendered in the following three figures b) xz -plane slice at $y=2.75$ cm, c) xy -plane slice at $z=0.25$, d) yz -plane slice at $x=-2.5$. Gray scale (units cm^{-1}) for all figures is shown in subplot b.

FIG. 3. Reconstruction of two point objects used for PSF measurements with $l_c = 0.1$. a) Three slices through the volume at $x=-2.5, y=2.75$ and $z=0.25$, combined with an isosurface at half maximum contrast ($\mu_a = 0.079$). b) xz -plane slice at $y=2.75$ cm. c) xy -plane slice at $z=0.25$, d) yz -plane slice at $x=-2.5$. Gray scale (units cm^{-1}) for all figures is shown in subplot b.

FIG. 4. a) Cross-sections for three values of l_c . b) Image dispersion histograms for three values of l_c .

FIG. 5. a) Image noise vs -FWHM of PSF as a function of the regularization constant (l_c) for $l_c = \{1000, 100, 10, 1, 0.1, 0.01, 0.001\}$ b) Image norm -vs- residual norm. c) The ratio of (object contrast)/(image noise) as a function of l_c .

FIG. 6. Comparison of images of objects with different size (diameter= $\{0.5, 1.0, 1.5\}$ cm) and equivalent intrinsic contrast ($\delta\mu_a = 0.15 \text{ cm}^{-1}$). a) Cross-sections for the three objects show that the peak signal decreases for objects smaller than the PSF of the instrument. b) Comparison of the volume integrated signal versus expected for an integration volume defined by $1.5 \times (\text{FWHM of PSF})$.

FIG. 7. A reconstruction of 15 objects indicates the spatial extent of the imaging domain of the instrument (field of view). Isosurfaces are drawn at % 50 peak differential contrast.

FIG. 8. Slices at three y values $\{1.5, 3, 4.5\}$ through the 15 object reconstruction shown in figure 7.

FIG. 9. a-d) Absorption slice images at $y=3$ cm, for four wavelengths, (gray scale bar in units of cm^{-1} e,f) Reconstructed concentrations of ICG and of india ink

FIG. 10. a)& b) Transillumination image obtained by summing images for all source positions for 690nm and 830nm respectively

FIG. 11. Data and fits based on semi-infinite diffuse wave solution to frequency domain data at 4 colors for measurements on human breast.

FIG. 12. Absorption and Scattering coefficients for a healthy human breast

FIG. 13. Differential image reconstruction of phantom target taped on to human breast. a) Three slices through the volume at $x=-2.5, y=2.75$ and $z=0.25$, combined with an isosurface at half maximum contrast ($\mu_a = 0.083$). b) xz-plane slice at $y=2.75$ cm. c) xy-plane slice at $z=0.25$, d) yz-plane slice at $x=-2.5$. Gray scale (units cm^{-1}) for all figures is shown in subplot b.

FIG. 14. Histogram of the voxel values for the *in vivo* phantom differential images. Three images are analyzed including; i) target on subject, ii) baseline variance in subject measurements, ii) baseline variance in intralipid measurements.

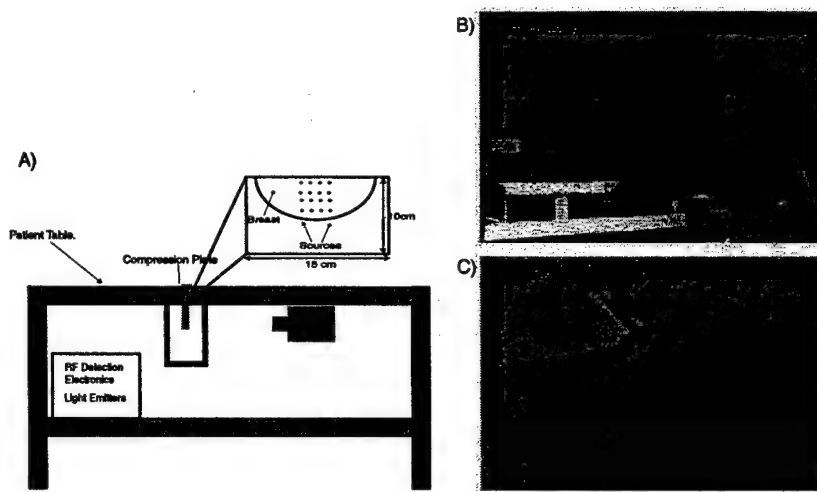


Figure 1, Three-Dimensional Diffuse... Joseph P. Culver, Medical Physics

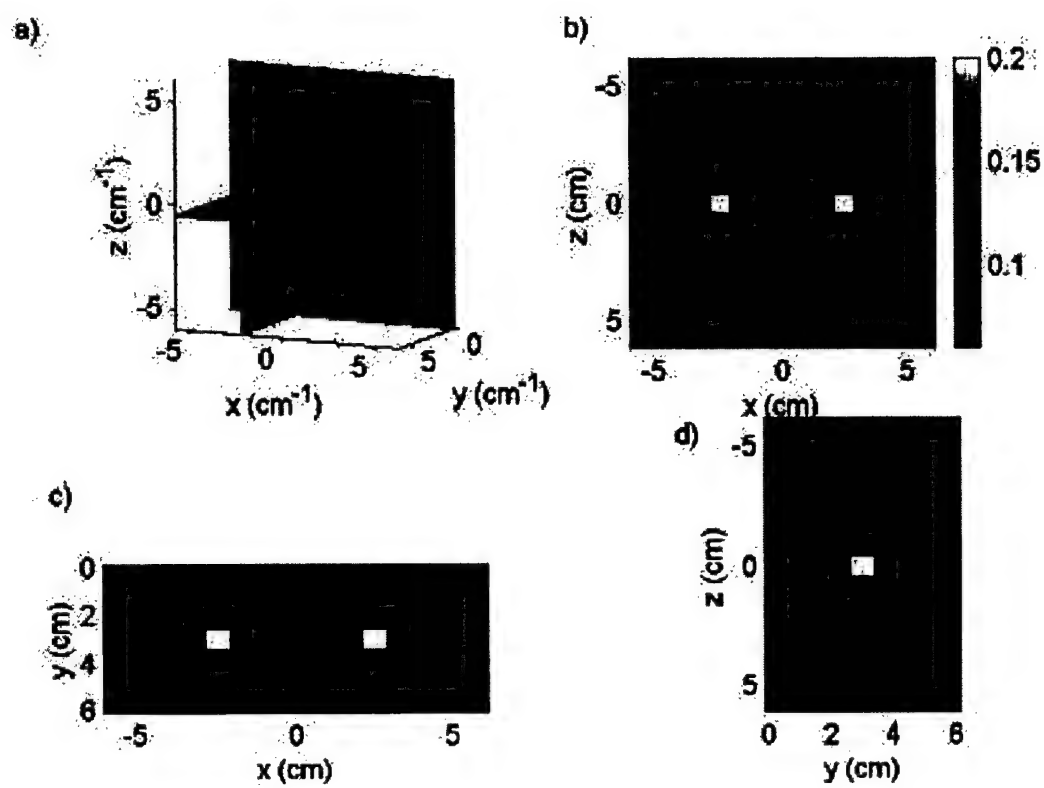


Figure 2, Three-Dimensional Diffuse... Joseph P. Culver, Medical Physics

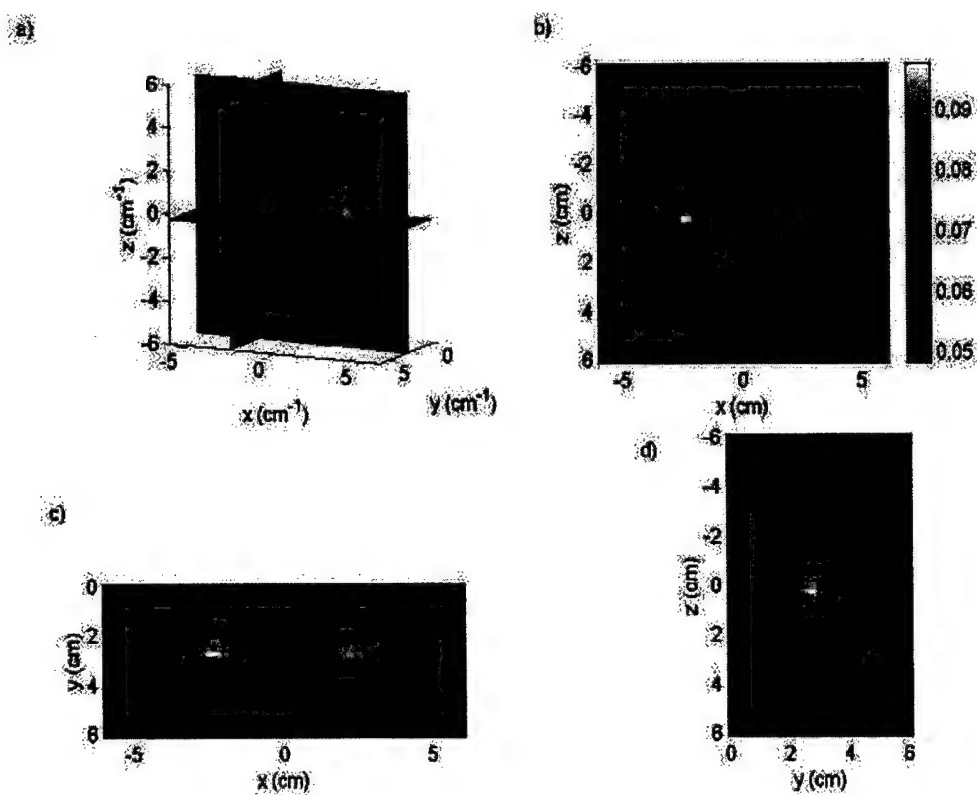


Figure 3, Three-Dimensional Diffuse... Joseph P. Culver, Medical Physics

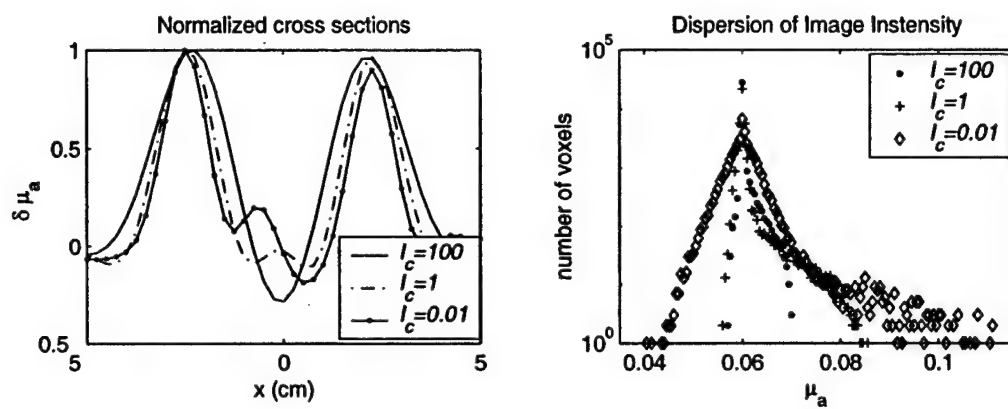


Figure 4, Three-Dimensional Diffuse... Joseph P. Culver, Medical Physics

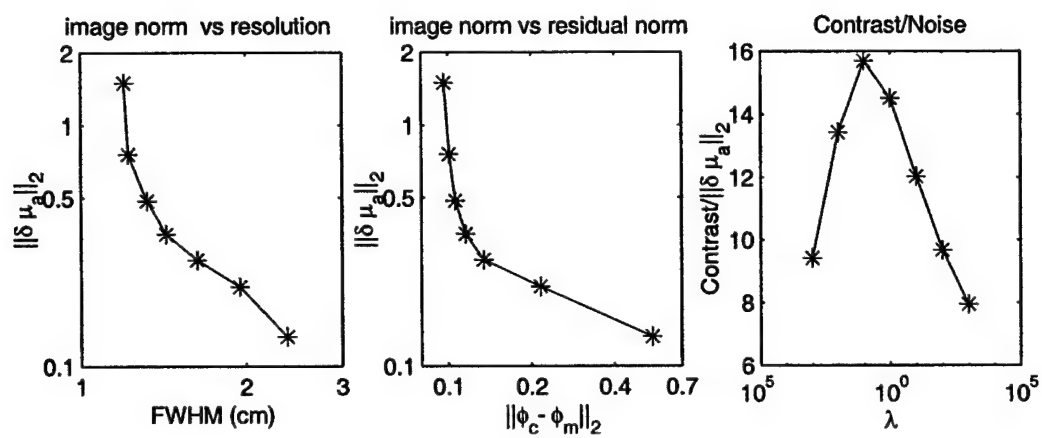


Figure 5, Three-Dimensional Diffuse... Joseph P. Culver, Medical Physics

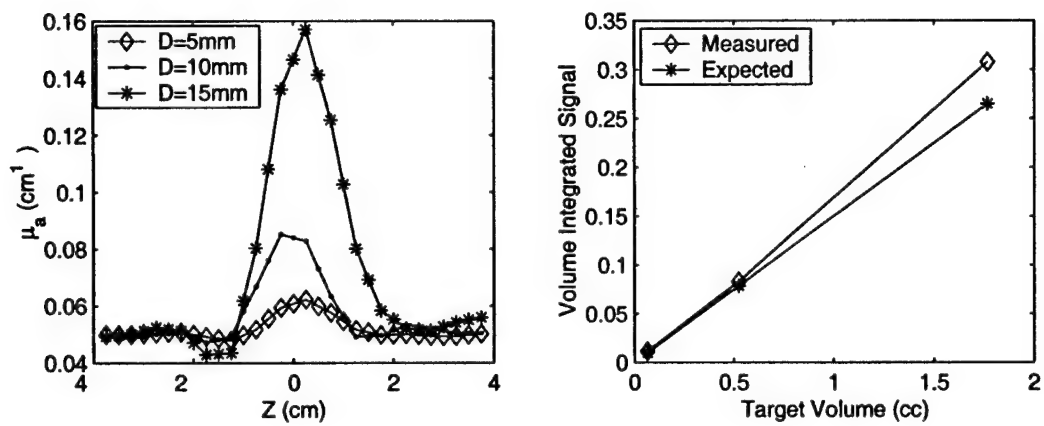


Figure 6, Three-Dimensional Diffuse... Joseph P. Culver, Medical Physics

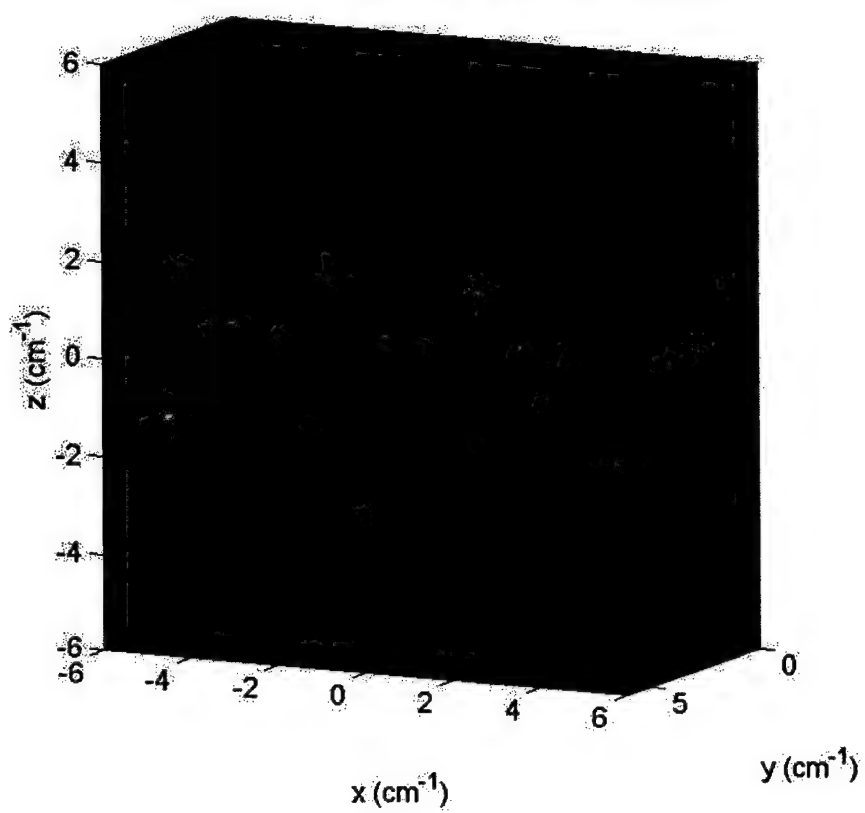


Figure 7 Three Dimensional Diffuse Joseph D. Culver, Medical Physics

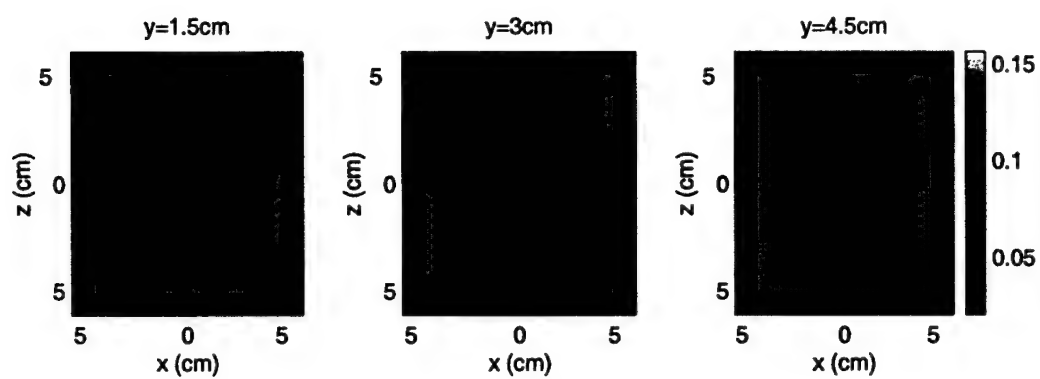


Figure 8, Three-Dimensional Diffuse... Joseph P. Culver, Medical Physics

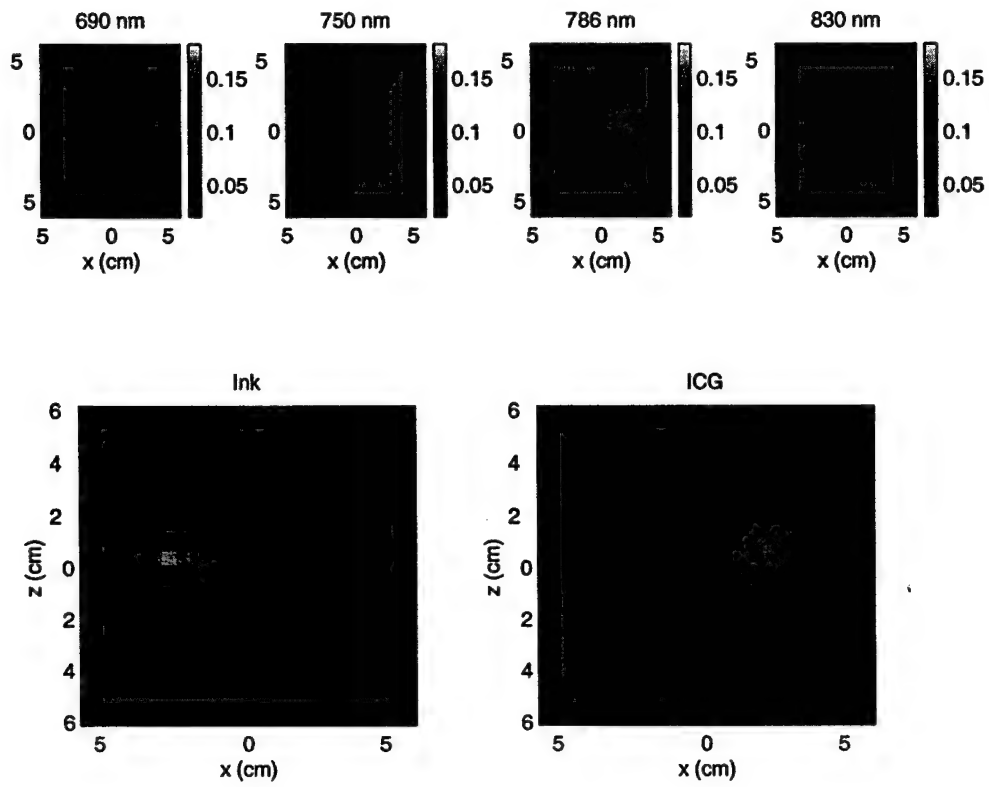


Figure 9, Three-Dimensional Diffuse... Joseph P. Culver, Medical Physics

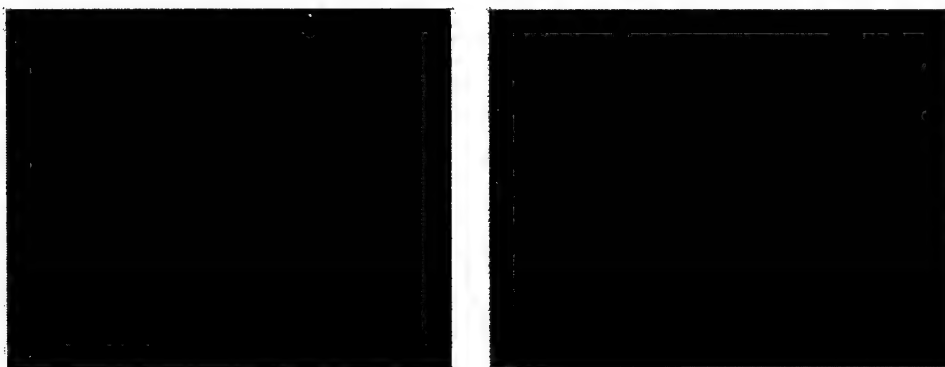


Figure 10, Three-Dimensional Diffuse... Joseph P. Culver, Medical Physics

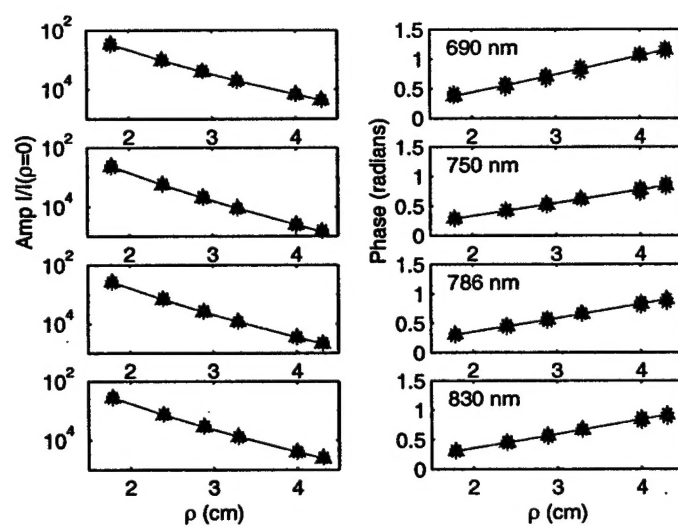


Figure 11, Three-Dimensional Diffuse... Joseph P. Culver, Medical Physics

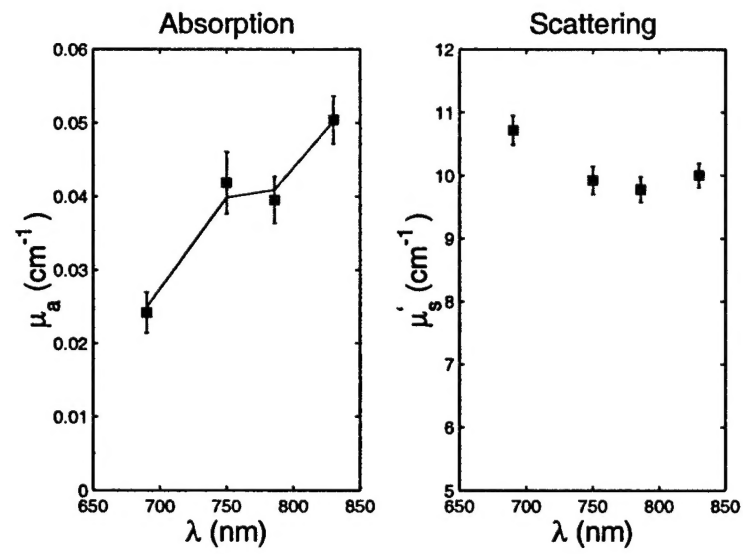


Figure 12. Three-Dimensional Diffuse... Joseph P. Culver. Medical Physics

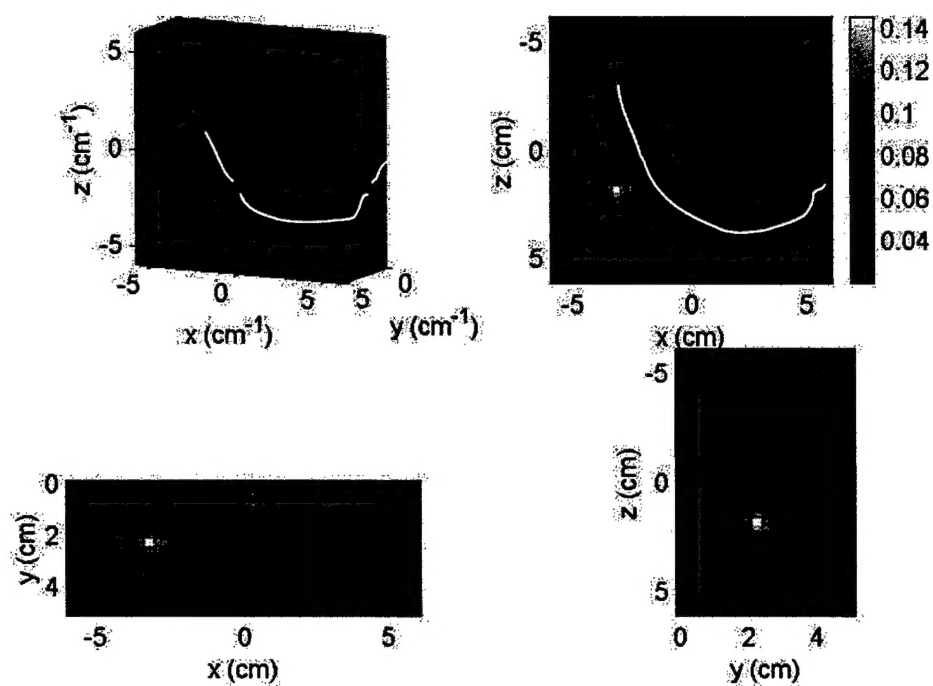


Figure 13, Three-Dimensional Diffuse... Joseph P. Culver, Medical Physics

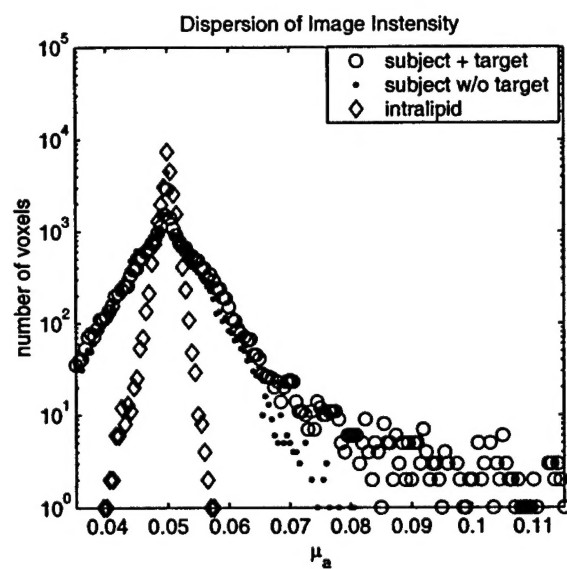


Figure 14, Three-Dimensional Diffuse... Joseph P. Culver, Medical Physics